Experimental constraints on the shock history of CI chondrites and Ryugu grains

Toru Nakahashi[1], Masaaki Miyahara[1,*], Akira Yamaguchi[2], Takamichi Kobayashi[3], Hitoshi Yusa[3], Masashi Miyakawa[3], Naotaka Tomioka[4], Yuto Takaki[1], Takaaki Noguchi[5], Toru Matsumoto[5,6], Akira Miyake[5], Yohei Igami[5], and Yusuke Seto[7]

[1]Graduate School of Advanced Science and Engineering, Hiroshima University, Higashi-Hiroshima, 739-8526, Japan.
[2]National Institute of Polar Research, Tokyo 190-8518, Japan.
[3]National Institute for Materials Science, Tsukuba 305-0044, Japan.
[4]Kochi Institute for Core Sample Research, X-star, JAMSTEC, 200 Monobe Otsu, Nankoku, Kochi 783-8502, Japan.
[5]Division of Earth and Planetary Sciences, Kyoto University, Kitashirakawaoiwake-cho, Sakyo-ku, Kyoto 606-8502, Japan.
[6]The Hakubi Center for Advanced Research, Kyoto University, Kitashirakawaoiwake-cho, Sakyo-ku, Kyoto 606-8502, Japan.
[7]Department of Geosciences, Osaka Metropolitan University, Sugimoto 3-3-138, Sumiyoshi-ku, Osaka 558-8585, Japan.

*Corresponding author: Dr. Masaaki Miyahara
Graduate School of Advanced Science and Engineering, Hiroshima University, Higashi-Hiroshima, 739-8526, Japan.
Postal code: 739-8526
Telephone: +81-824-24-7461
FAX: +81-82-424-0735
E-mail address: miyahara@hiroshima-u.ac.jp

Abstract

C-type asteroids, which make up a significant portion of the main belt asteroids, are believed to be composed of materials similar to CI and CM carbonaceous chondrites. In this study, we conducted shock recovery experiments on the Orgueil CI and CI affinity Yamato 980115 CY (partly dehydrated CI) chondrites to examine their mineralogical and textural changes under impact conditions. Our results indicate that weak shock pressures below approximately 4 GPa do not produce significant shock metamorphic features, supporting the current interpretation that most Ryugu grains experienced shock pressures within this range. Above approximately 4 GPa, dehydration and degassing of Mg-Fe phyllosilicates and carbonaceous materials become dominant, leading to rock fragmentation along cracks. Rock melting initiates above approximately 10 GPa, leading to the formation of frothy regions composed of iron-rich amorphous material containing numerous small, rounded voids. These voids are generated by the degassing of volatiles (H_2O and CO_2) during shock-induced melting or vitrification. These findings suggest that the regolith layer of asteroid Ryugu was primarily formed by the reassembly of rock fragments exfoliated by impacts without undergoing strong shock metamorphism. However, highly shocked materials may be buried beneath the regolith layer, highlighting the need for further investigations into the interiors of C-type asteroids to better understand their thermal and impact histories.

Keywords: Asteroid Ryugu, CI chondrite, Impact process, Shock experiment, Shock metamorphism

Highlight:

- Impact-induced petrographic and mineralogic changes on CI chondrites are revealed.
- Shock pressures below ~4 GPa cause little to no structural changes.
- Dehydration and degassing of Mg-Fe phyllosilicates become significant above ~4 GPa.
- Melting and formation of iron-rich amorphous material occur above ~10 GPa.
- Ryugu's regolith formed primarily through reassembly of impact-fragmented material.

1. Introduction

About 80% of the asteroids in the main belt are C-type, and their spectra are similar to those of the hydrated CI-CM chondrites (Bus and Binzel, 2002). CM chondrites are more commonly recovered, while CI chondrites are rare due to their friability and weathering susceptibility. Hayabusa2 samples from the C-type asteroid closely resemble CI chondrites in petrology, mineralogy, and geochemistry (e.g., Ito et al., 2022; Nakamura et al., 2023; Yokoyama et al., 2023). Boulders with layered structures dominate Ryugu's surface, interpreted as evidence of shock metamorphism, suggesting that Ryugu is a rubble-pile asteroid formed through repeated impact events and reassembly (Tachibana et al., 2022; Watanabe et al., 2019).

Impacts play a crucial role in the physical and chemical evolution of asteroids, inducing deformation, dehydration of hydrous minerals, and structural modifications in organic matter (e.g., Furukawa et al., 2009; Nakamura et al., 2000; Wakita et al., 2022). The shock pressure and temperature conditions experienced by meteorites and asteroid regolith particles can be evaluated by comparison with laboratory shock experiments conducted on petrologically similar materials (Miyahara et al., 2021; Nakamura et al., 2000; Ohtani et al., 2022; Ono et al., 2023; Stöffler et al., 2018; Tomeoka et al., 1999). However, due to their high volatile content, CI chondrites have rarely been used in shock recovery experiments, as the rapid post-shock heating often causes explosive dispersion of the sample.

We have developed an experimental technique for recovering shocked CI chondrite samples that minimizes the required amount of starting material and significantly reduces sample dispersion losses. This study aims to establish a shock classification scale specifically for CI chondrites based on shock recovery experiments. Using the Orgueil CI and Yamato (Y) 980115 CY chondrites as starting materials, we investigated microstructural and chemical changes induced by shock pressures ranging from ~5 to ~45 GPa. The Y 980115 CY chondrite is chemically/petrographically similar to the CI chondrites, but a bit thermally metamorphosed (King et al., 2019) and thus is classified as a CI affinity (Ebihara et al., 2025).

Additionally, we applied the results of our experimental framework to assess the shock histories of Ryugu grains, evaluating whether their shock features align with those observed in our experimentally shocked CI/CY chondrites. This study provides essential constraints on the response of CI/CY chondrites to impact events and sheds light on the fragmentation and reassembly processes of C-type asteroids such as Ryugu.

2. Materials and experimental methods

2.1 Materials

Both Orgueil CI and Y 980115 CY chondrite samples were allocated from the National Institute of Polar Research (NIPR), Japan. The allocated Orgueil CI sample is granular (< ~1 mm; Fig. S1a) and was placed 3 mm below the impact surface in stainless steel (SUS 304) containers. The granular samples were hand-pressed and their thickness measured with a vernier micrometer, yielding a bulk density of 1.72–2.28 g/cm³ (Table 1), between that of Orgueil CI and Murchison CM2 chondrites. Finally, the sample chamber was closed and secured with a threaded cap.

Y 980115 CY chip samples were cut from a chunk sample using a wire saw without water at NIPR (Fig. S2a). Both sides were polished using 3MTM diamond lapping film without water. Disc samples (φ = 6 mm) were extracted from the doubly polished samples using an ultrasonic cutting machine. The disk sample was placed in the sample chamber of the SUS 304 container. The density of individual Orgueil and Y 980115 samples was calculated by measuring their thickness, diameter, and weight (Table 1).

A0304, C0055, and C0230 Ryugu grains were provided by the Japan Aerospace Exploration Agency (JAXA), Japan. A0304 and C0230 grains were embedded in epoxy resin and polished using the procedures outlined below. C0055 grain had already undergone embedding and polishing, having been previously analyzed in Nakamura et al. (2023). A dataset of AP0042 Ryugu grain, which was analyzed by the Hayabusa2 Initial Analysis “Sand” Team, was partly used in this study.

2.2 Shock experiments

The shock experiments used a 30 mm bore propellant gun installed at the National Institute for Materials Science (NIMS), Tsukuba, Japan. A 2 mm thick SUS 304, tungsten (W), or polyethylene (PE) flyer plate was attached to the head of a projectile (Table 1) and impacted the SUS 304 containers. The velocity just before the impact was measured by the magneto flyer method (Kondo et al., 1977). The peak shock pressure was calculated by the impedance match method using the known Hugoniot data for the container, flyers, and sample. The compiled data for SUS 304, W, and PE are from Marsh (1980) and for the Murchison CM2 carbonaceous chondrite from Anderson and Ahrens (1998).

Since the Hugoniot data for CI/CY chondrites have not yet been determined, we adopted the Hugoniot parameters of Murchison CM2, which has the most comparable bulk density (2.15–2.40 g/cm³) and porosity (18.8–24.9%) (Macke et al., 2011) to those of the compressed granular Orgueil CI (1.72–2.28 g/cm³) and platy CY chondrite samples (1.75–1.99 g/cm³) (Table 1). Although we could not directly measure the porosity of the compressed granular Orgueil CI samples, porosity is closely correlated with bulk density. Therefore, it is reasonable to assume that the porosities of the

compressed Orgueil CI samples also lie between those of Orgueil CI and Murchison CM2 chondrites.

2.3 Sample analysis

The SUS 304 containers were recovered after individual shock experiments and were sliced open with a precision lathe to extract samples. The reverberation of a shock wave occurs at the boundary between the high-impedance container and the low-impedance chondrite sample, by which the sample in contact with the container may be subject to local spikes of pressure and temperature and/or reaction (Knudson et al., 2004). Therefore, from the removed sample, the central portion was hollowed out and embedded in epoxy resin. The detailed sample polishing procedure is described in Yamaguchi et al. (2023).

Backscattered electron (BSE) images were taken using a field-emission gun scanning electron microscope (FE-SEM): JEOL JSM-7100F installed at NIPR for the detailed texture observations of polished samples at an accelerating voltage of 15 kV after carbon coating. The polished sample was imaged by BSE, and individual images were merged using SEM software.

The open crack density and melting area observed in each sample were measured using the merged BSE images and the ImageJ image processing application. To determine the open crack density, we measured open cracks with a width of at least 0.25 μm and a length of at least 7.5 μm, following the definition established by Sekigawa et al. (2009). Elemental mapping and qualitative analysis of the samples were performed using an X-ray energy dispersive spectrometer (EDS), Oxford X-Max attached to the FE-SEM.

Parts of the sample were excavated using a focused ion beam (FIB) system, HITACHI SMI4050, which is equipped with a microprobe system, at the Kochi Institute for Core Sample Research, Japan Agency for Marine-Earth Science and Technology (JAMSTEC) for transmission electron microscopy (TEM) observation. The gallium ion beam was accelerated to 30 kV during the sputtering of the sample by the FIB. The resulting foils are approximately 100 nm thick.

A JEOL JEM-2100F field emission TEM at Tohoku University, operating at 200 kV and equipped with a JEOL EDS detector system, was used for conventional TEM observation and selected area electron diffraction (SAED) pattern analysis. We determined the chemical composition of each mineral in scanning TEM (STEM) mode using the EDS detector. The chemical compositions were corrected using experimentally determined *k*-factors for San Carlos olivine, pyrope, and albite.

3. Results

3.1 Petrologic descriptions of starting materials

The starting material Orgueil CI chondrite consists almost entirely of matrix, including Mg-Fe phyllosilicates (saponite and serpentinite: hereafter Mg-Fe phyls), iron (Fe)-oxides, sulfides, carbonates, and carbonaceous materials. Distinguished textures associated with shock metamorphism, such as subparallel cracks and melts, are not observed (Fig. S1b, S1c). The matrix consists mainly of fibrous Mg-Fe phyls assemblages. Fine-grained Fe-oxides and -sulfides are embedded in the Mg-Fe phyls assemblages (Fig. S1d). Numerous clusters of euhedral magnetite grains form a framboidal structure (framboidal magnetite cluster: FMg). Many interstitial spaces exist among the Mg-Fe phyls assemblages, with carbonaceous materials filling some of the interstices (Fig. S1e).

Another starting material, Y 980115 CY chondrite, is a chunk sample consisting of fragments several mm in size (Fig. S2b). Similar to Orgueil CI, Y 980115 CY consists almost entirely of matrix, including Mg-Fe phyls, Fe-oxides, sulfides, carbonates, and carbonaceous materials (Fig. S2c, S2d). Distinguished shock metamorphism textures are absent.

3.2 Shocked Orgueil CI chondrite

Seven samples were successfully recovered after the shock experiments (Table 1). FE-SEM observations show that some irregular fractures were observed in the sample shocked at 4.6 GPa (Fig. 1a, S3a). The outlines of some FMgs were slightly deformed and individual magnetite grains in some clusters were slightly dispersed (Fig. 1a). Based on the FE-SEM observations, there are few differences in texture between the samples shocked at 4.6 GPa and 11.4 GPa (Fig. 1a, S3a, S3b).

A portion of the sample shocked at 11.4 GPa was excavated using FIB, and a TEM foil was prepared from it. Bright-field (BF) TEM images of the foil show that the matrix is slightly compressed in part and has fewer interstices than the starting material, while retaining its original microstructures (Fig. 2a). Fibrous Mg-Fe phyls overlap due to compression, making it difficult to observe lattice fringes of individual crystals. In some areas, the Mg-Fe phyls and carbonaceous material are compacted together, making it difficult to distinguish individual materials (Fig. 2b). Most of the micro/nano carbonaceous globules retain their original spherical shapes (Fig. 2b), although they are included in the slightly compacted matrix.

Distinct shock metamorphic microstructures were observed in the samples shocked at ~20 GPa or higher. Irregular and subparallel cracks were frequently observed in the sample shocked at 21.0 GPa (Fig. 1b, S3c). Subparallel cracks formed in fine-grained Mg-Fe phyls and carbonaceous material, but not in coarse-grained carbonates or Fe-sulfides (FeS). The outlines of FMgs are elongated parallel to the subparallel cracks

(Fig. 1b). In some FMgs, individual magnetite grains are completely dispersed.

In the sample shocked at 32.2 GPa (Fig. 1c), subparallel cracks developed more densely compared to the sample shocked at 21.0 GPa. A region exhibiting such densely spaced subparallel cracks was selected for detailed observation using TEM. Vitrified Mg-Fe phyls and those that remained crystalline without undergoing amorphization are irregularly aligned along the fractures (Fig. 2c). The individual grains that comprised FMgs are completely separated. Magnetite and FeS grains are arranged along the subparallel cracks. Micro/nano carbonaceous globules are flattened along the subparallel cracks. Amorphous material containing numerous froths (hereafter referred to as a frothy region) is present within the interstices of the subparallel cracks (Fig. 2d). In some areas of the sample, where the original characteristics of CI chondrites disappeared: there are no subparallel cracks; instead, frothy regions are present (Fig. 1d, S3d). TEM observations reveal that such parts consist of amorphous material, fine-grained spherical hematite (< ~1 μm across), FeS, and froths (Fig. 2e). EDS analysis indicates that the amorphous material is a mixture consisting mainly of decomposed and/or vitrified Mg-Fe phyls and sulfides (Fig. 2f).

At 36.4 GPa, subparallel cracks are rare, while frothy regions dominate. In some areas, the frothy regions occur as a vein (Fig. S3e). Most of the shocked samples at 40.5 and 45.0 GPa contain frothy regions (Fig. 1e, 1f). Some froths have an outline that appears to be stretched in a particular direction (Fig. 1e). Some coarse-grained FeS grains have bubbles (Fig. S3f).

3.3 Shocked Y 980115 CY chondrite

Three samples shocked at ~10 to ~30 GPa were successfully recovered (Table 1). Similar to the Orgueil CI chondrite shocked at ~5 and ~10 GPa, no significant changes in the petrographic texture were observed in the BSE images between the starting material and the Y 980115 CY chondrite shocked at 10.7 GPa (Fig. 3a). A few short subparallel cracks and slightly deformed FMgs were also found in some areas of the 10.7 GPa sample (Fig. 3a).

In both of the samples shocked at 22.3 and 32.5 GPa, dense subparallel cracks developed (Fig. 3b, 3c). FMgs are deformed, and individual grains are dispersed. BF-TEM images of the sample shocked at 22.3 GPa show that the matrix is heterogeneously compacted and has fewer interstices compared to the starting material (Fig. 4a). It is difficult to distinguish individual packets of Mg-Fe phyls in the matrix. Several short subparallel and irregular cracks are filled with frothy regions (Fig. 4a, 4b).

Even in the sample shocked at 22.3 GPa, some Mg-Fe phyls have survived due to heterogeneous compaction (Fig. 4a, 4b, 4c). Lattice fringes with a periodicity of ~1

nm, which can be assigned to the (001) planes of dehydrated saponite, were observed in some areas of the matrix (Fig. 4c). In some parts of the sample shocked at 32.5 GPa, frothy regions are present (Fig. 3d). This frothy region resembles that found in the shocked Orgueil CI chondrite (Fig. 4d). The chemical compositions of the Mg-Fe phyls in the starting material, the interstitial frothy region between the cracks in the sample shocked at 22.3 GPa, and the frothy region in the sample shocked at 32.5 GPa were determined by STEM-EDS. Based on the chemical compositions, the amorphous material is a mixture of decomposed and/or vitrified Mg-Fe phyls and carbonaceous material (Fig. 4e).

3.4 Ryugu grains

Among the A0304, C0055, and C0230 Ryugu grains, subparallel cracks were widely observed only in the C0055 grain (Fig. 5a). Some of the cracks are oblique to the subparallel cracks. Crack densities of the A0304, C0055, and C0230 Ryugu grains are shown in Table S1. Typical petrologic textures of the A0304 and C0230 grains are shown in Figure S5.

Cracks extend across some FMgs in the C0055 Ryugu grain. When subparallel cracks intersect FMgs, minimal displacement is observed along the cracks (Fig. 5b). The cross section of the crack was excavated by FIB for TEM observation. BF-TEM images show that the matrix is heterogeneous. In some areas, the Mg-Fe phyls packets are loosely assembled with interstitials. In contrast, in other areas, it is difficult to identify individual packets of fine-grained Mg-Fe phyls because they are compacted and become dense. The compacted matrix is torn off along the crack (Fig. 6a). There is no evidence of vitrification, melting or decomposition of the Mg-Fe phyls on either side of the open cracks.

In cases where cracks are oblique to the subparallel cracks, FMgs are sheared along the cracks (Fig. 5c). The fine-grained Mg-Fe phyls packets are strongly compacted between magnetite grains. In contrast, the packets of coarse-grained Mg-Fe phyls are bent and folded around the magnetite grains, thus leading to form interstices (Fig. 6b). There is no clear evidence for shear-induced heating such as vitrification of Mg-Fe phyls.

Some cracks developing obliquely to the subparallel cracks occur along the long axis of coarse-grained Mg-Fe phyls packets. The packets appear to be slightly sheared (Fig. 5d). The coarse-grained serpentine is deformed along the (001) plane, and the individual (001) planes are pulled apart (Fig. 6c, 6d). A frothy region is present between the detached (001) plane of serpentine.

4. Discussion

4.1 Shock metamorphic texture

4.1.1 Elastic deformation dominant region (< ~10 GPa)

Significant shock metamorphic textures were not observed in both the Orgueil CI and Y 980115 CY chondrites shocked at less than ~10 GPa, except for the compression of Mg-Fe phyls assemblages and carbonaceous materials (Fig. 1a, 2a, 2b, 3a). Rocks with high porosity exhibit a distinct strain–stress behavior compared to low-porosity rocks: they deform readily under low stresses due to pore collapse, resulting in a rapid increase in strain, followed by a sudden drop in strength and large deformation (Jaeger et al., 2009). In the CI/CY chondrites, no distinct shock metamorphic textures indicative of plastic deformation are observed below approximately 10 GPa. The compaction of the matrix is progressive, indicating that in this shock pressure range, elastic deformation is more dominant than plastic deformation (Fig. 7a). Because of the high degree of compaction in the range below ~10 GPa, shock-induced heating is likely to be most pronounced in this range.

4.1.2 Plastic deformation/tensile fracture dominant region (~10–30 GPa)

Plastic deformation becomes dominant beyond approximately 10 GPa (Fig. 7a). The shear deformation of the matrix is clearly confirmed by the deformation of FMgs and the development of subparallel cracks (Fig. 1b, 1c, 3b, 3c). Assuming that the outline of FMg is nearly spherical, its aspect ratio (the ratio of its short axis to its long axis) may serve as a strain marker related to shock pressure. When rocks experience shear deformation, displacement occurs along the shear plane. In Ryugu grains, there are also fracture planes with displacement, which are traces of shear failure during shock metamorphism (Tomioka et al., 2023).

Subparallel cracks can be produced by two causes: i) shear stress, ii) tensile stress. In the first cause, shear failure occurs by sliding obliquely to the shock front when applied shock pressure exceeds the elastic limits of the CI/CY chondrites. The shear failure results in displacement and melting, when frictional heating at the shear planes is significant. However, in the Ryugu grains, it is unlikely that shear failure was a dominant crack formation mechanism, because there are few cracks with displacement in the experimentally shocked CI/CY chondrites (Fig. 1b, 1c, 3b, 3c).

Rocks with high porosity exhibit lower tensile stresses than those with low porosity (Jaeger et al., 2009). The Ivuna and Orgueil CI chondrites have very low tensile strength (0.7–2.8 MPa) (Pohl and Britt, 2020; Tsuchiyama et al., 2008). From these, we favor that tensile stress was the primary cause for the crack formation in the matrix. The CI/CY chondrites were compressed by the propagation of the shock wave generated at the impact surface, and the pressure was released after the arrival of the reflected expansion wave. During this pressure release process, the CI/CY chondrites

were subjected to tensile stress, leading to the formation of subparallel cracks perpendicular to the stress direction.

Frothy regions are present along micro-order cracks in the sample shocked above approximately 20 GPa (Fig. 2d, 4b). The amorphous material in the frothy regions consists of vitrified/melted Mg-Fe phyls and carbonaceous minerals (Fig. 2f, 4e). The former and the latter would have released interlayer water (OH^-) and OH^+ and carbon dioxide, respectively, producing froths. The crack density gradually increases up to a shock pressure of approximately 20 GPa (Fig. 8a). Beyond this threshold, the crack density rises drastically and reaches saturation around 30 GPa. This sharp increase is likely attributed to the expansion pressure caused by H_2O degassing from Mg-Fe phyls and CO_2 degassing from carbonaceous materials that commence at around 20 GPa. This observation aligns with the findings from the shock experiments on the CM chondrites (Tomeoka et al., 1999; Tomioka et al., 2007) and the mid-infrared spectra analysis of the samples recovered from the experiments (Morlok et al., 2010). All these previous works indicate that the onset of dehydration and degassing took place at approximately 20 GPa.

Considering the dehydration temperatures of saponite and serpentine (Akai, 1992; Ball and Taylor, 1963; Brindley and Hayami, 1963; Cattaneo et al., 2003; Weber and Greer, 1965), the temperature at a shock pressure of approximately 20 GPa can be estimated to be at least above 473 K. At temperatures above ~500 K, the organic matters in the carbonaceous chondrites begin to decompose and various gases including CO_2 and H_2 are thought to be produced (e.g., Francioso et al., 2005). Such phenomena probably also contributed to the development of cracks in the matrix.

4.1.3 Melting dominant region (> ~30 GPa)

The chemical compositions of the amorphous materials in the frothy regions are rich in iron compared to those of Mg-Fe phyls in the starting materials (Fig. 9a, 9b). Hematite grains are present in the frothy regions (Fig. 2e, 4d). A small amount of sulfur is also found in the amorphous materials (Fig. 2f, 4e). The presence of a bubble in the FeS grain indicates melting (Fig. S3f). The frothy region likely consists of quenched melts of Mg-Fe phyls accompanied by magnetite and FeS. Hematite likely crystallized from the melts during the quenching process (Fig. 2e, 4d). For samples shocked above approximately 30 GPa, the volume ratio of the melt increases rapidly (Fig. 8b), making it difficult for cracks to form.

According to the heating experiments of serpentine (Akai, 1992; Ball and Taylor, 1963; Brindley and Hayami, 1963; Cattaneo et al., 2003; Weber and Greer, 1965), adsorbed water is released below 473 K. Between 873 and 1073 K, removal of OH groups within the crystal structure occurs, leading to structural collapse and the

formation of an amorphous phase. Above 1073 K, forsterite and enstatite crystallize from the amorphous material. Saponite decomposes to enstatite above 1100 K after dehydration around 473 K (Akai, 1992). The melting temperature of magnetite at ambient conditions is 1868 K (Walker and Tarn, 1990). Based on the eutectic melting curve for the reaction Mg_2SiO_4-$MgSiO_3$, the melting temperature is about 3000 K at 26 GPa (Presnall et al., 1998). In the frothy regions (Fig. 2e, 4d), neither forsterite nor enstatite was identified. Furthermore, magnetite—abundant in the host rock—is rarely observed in these regions. The amorphous material that constitutes most of the frothy regions is richer in iron compared to the Mg-Fe phyls in the host rock (Fig. 9a, 9b). The iron-rich composition of the amorphous material suggests that magnetite may have melted and mixed with amorphous phases derived from Mg-Fe phyls. Therefore, the temperature in the frothy regions likely exceeded approximately 1900 K and may have reached up to approximately 3000 K.

4.2 Differences between CI and CY chondrites

The Y 980115 CY chondrite is akin to the CI chondrites heated to 500–750 °C and has distinct characteristics to both CI and CM chondrites (Ebihara et al., 2025; Ikeda, 1992; King et al., 2019). The bulk density, porosity, and H_2O abundance of Orgueil CI are respectively 1.57 g/cm^3, 34.9%, and 18.3wt% (King et al., 2015; Macke et al., 2011). Although the bulk density and porosity of the Y 980115 CY chondrite have not been determined, they are thought to be slightly higher and lower than those of the Orgueil CI chondrite, respectively, because it is a thermally metamorphosed CI chondrite. There is a difference in H_2O abundance between Orgueil CI (18.3wt%) and Y 980115 CY (11.6wt%) (Braukmüller et al., 2018). This causes them to have different shock impedances, affecting pressure-temperature path, and shock-induced texture. However, the effect of H_2O abundance on the degree of shock metamorphism is actually not significant because there are few differences in crack densities and melt volume ratios between Orgueil and Y 980115 chondrites (Fig. 8). If projectiles with the same size, component, and velocity collide with the parent bodies of CI/CY chondrites, their modes of deformation would be similar.

4.3 Comparison with natural impacts

The matrices of CI/CY chondrites mainly consist of loosely aggregated fine-grained Mg-Fe phyls. In all meteorites, CI/CY chondrites exhibit the highest bulk porosity due to the high volume fraction of the matrix (Macke et al., 2011). This high porosity led to large volume reduction during impacts compared to less-porous meteorites, causing high post-shock heating, heterogeneous temperature distributions, and relative motions of the components that shear and collide with each other (e.g., Kieffer, 1971, 1975). Accordingly, the estimation of not only shock pressure but also

shock-induced heating is crucial, because the dehydration, decomposition, and degassing of Mg-Fe phyls and carbonaceous material are temperature-dependent processes.

In collisions between asteroids, the shock pressure is increased by the concentric propagation of shock compression waves from the point of collision, followed by pressure release by the rarefaction waves arriving later. As a result, the peak shock pressure is reached with a single shock compression wave (Fig. 7c). In contrast, in a shock experiment using a stainless-steel container, the shock compression wave is repeatedly reflected at the boundary between the sample and the container mainly due to their impedance difference, and therefore the shock pressure increases gradually to reach the peak pressure (Fig. 7b). Even though the final peak shock pressures are the same, a single shock compression wave and a shock compression wave with repeated reflections have different internal energies and cause different temperature histories (Fig. 7b, 7c). Therefore, in order to apply the results of the present shock experiments with the CI/CY chondrites to asteroid impact phenomena, it is necessary to accurately evaluate the reflections of the shock compression waves generated at the sample-vessel boundary and the total amount of internal energy associated with them.

An internal energy increase at each step of shock-wave reflections can be calculated using the Rankine–Hugoniot equation of states and expressed as:

$$E_n - E_{n-1} = (P_n - P_{n-1})(V_{n-1} - V_n)/2 \qquad \text{eq. (1)}$$

where E_n, P_n, and V_n are internal energy, pressure, and the volume of the sample at the n-th reflection of the shock compression wave, respectively. The shock pressure (P_n) paths of the Orgueil CI and Y 980115 CY chondrites in the containers can be calculated using their Hugoniot data, such as the bulk sound velocity and the dimensionless parameter. However, the Hugoniot data of the CI/CY chondrites have not been determined.

Compressive behavior (shock impedance) is defined as the product of the density of the material and the shock wave velocity. In the literature, the bulk-density and porosity of Orgueil CI are, respectively, 1.57 g/cm^3 and 34.9% (Macke et al., 2011), whereas those of Murchison CM2 2.15–2.40 g/cm^3 and 18.7–24.9% (Macke et al., 2011). On the other hand, the average densities of Orgueil and Y 980115 enclosed in the containers respectively are 2.03 g/cm^3 (n = 7) and 1.85 g/cm^3 (n = 4) (Table 1). The densities of the Orgueil CI and Y 980115 CY chondrites are higher than those described in the literature, because the chondrites were pressed into the container with

a hand press. The bulk densities and porosities of Orgueil CI and Y 980115 CY can be regarded as the analog of Murchison CM2. The sizes and thicknesses of the containers and samples are almost the same between the present shock experiments and those by Tomeoka et al. (1999). Hence, the shock pressure (P_n) path of Orgueil CI and Y 980115 CY chondrites in the container and the sum of internal energy can be adopted from those of Murchison CM2 (Tomeoka et al., 1999).

The total internal energy increase by the reflection of the shock compression wave can be converted to temperature as follows (Horie and Sawaoka, 1993):

$$E = \int_{T0}^{T} Cp(T)dT \qquad \text{eq. (2)}$$

where T_0, T, and $C_p(T)$ are the initial temperature, the temperature after shock, and the heat capacity, respectively. By using the equation (2) and the total internal energy increase calculated by Tomeoka et al. (1999), we may estimate post-shock temperatures in natural impact phenomena of the CI/CY chondrite parent bodies. However, there are no adequate heat capacities for the CI/CY chondrites. In this study, pressure estimation was conducted by comparison of waste heat energies for reflected shock waves and a single shock wave, as calculated in Tomeoka et al. (1999).

At shock pressures below approximately 20 GPa, subparallel cracks likely form in response to tensile stress during depressurization (Fig. 8a). In contrast, above approximately 30 GPa, the melted area expands significantly (Fig. 8b). For reflected shock waves at pressures of approximately 20 GPa and 30 GPa, the waste heat energies are approximately 145 J/K and 280 J/K, respectively, equivalent to those at approximately 4 GPa and 10 GPa for single shock waves (Fig. 7a). This suggests that, in CI/CY chondrite parent bodies, rock fragmentation along rocks becomes significant above approximately 4 GPa, while rock melting initiates above approximately 10 GPa.

There is a difference of several orders of magnitude in the duration of the compression stage between shock recovery experiments and natural impact events: the former lasts only a few microseconds, while the latter can last several seconds (e.g., Hu and Sharp, 2022). In highly porous rocks, much of the impact energy is consumed by the collapse of pores, which contributes more to an increase in temperature than to pressure. Therefore, the formation of high-pressure minerals is not expected in CI/CY chondrites. Indeed, no high-pressure minerals have been reported in these chondrites (Tomioka and Miyahara, 2017). Furthermore, shock-induced amorphization of anhydrous minerals such as maskelynitization are also absent, we consider that the duration of the high-pressure condition does not need to be taken into account in these cases.

In contrast, the formation of subparallel cracks and melting is attributed to the high temperatures generated by pore collapse. The waste heat energy achieved under a given pressure corresponds to the maximum temperature after pressure release, and both subparallel crack density and melt area fraction are strongly dependent on this temperature. While the shorter heating duration in shock experiments is unlikely to cause major differences in crack density or melt area fraction, the values obtained experimentally under the estimated pressure conditions should be regarded as minimum estimates.

4.4 Application to Ryugu grains

The shock pressures experienced by the A0304, C0055, and C0230 Ryugu grains can be estimated, based on the shock metamorphic textures found in the recovered CI/CY chondrite samples after shock experiments. In the A0304 and C0230 Ryugu grains, deformation of FMgs, melting of the matrix, dense cracks, and the displacement along the cracks were not observed (Fig. S5). In contrast, subparallel cracks widely developed in the C0055 Ryugu grain (crack density: 697 mm^{-2}) (Fig. 5, Table S1). TEM observations of the Ryugu grains reveal that the fine-grained Mg-Fe phyls assemblages and carbonaceous material were slightly compacted (Fig. 6a, 6b) and the coarse-grained Mg-Fe phyls were slightly deformed along cracks (Fig. 6c).

The shock recovery experiments of the CI/CY chondrites show that the crack density increased approximately linearly in the range of shock pressures from ~0 to ~20 GPa (Fig. 8a). As discussed in the former chapter, when considering the waste heat energy, it is estimated that approximately 20 GPa in the shock experiment corresponds to approximately 4 GPa in a natural impact (Fig. 7a). Therefore, the relationship between crack density and shock pressure observed in the 0–20 GPa experimental range can be approximately applied to a 0–4 GPa natural shock environment. Based on this assumption, the crack density of 697 mm^{-2} observed in the C0055 Ryugu grain can be roughly translated to a shock pressure of approximately 0–2 GPa under natural conditions. The crack densities of the A0304 and C0230 Ryugu grains are 185 and 285 mm^{-2}, respectively (Table S1), similar to the unshocked CI/CY chondrites. Hence, the shock pressures that the A0304 and C0230 Ryugu grains experienced are estimated to be nearly 0 GPa.

In the C0055 Ryugu grain, frothy regions are present between the packets of deformed coarse-grained Mg-Fe phyls (Fig. 6c, 6d). The estimated shock pressure of approximately 0–2 GPa is lower than the pressure at which interlayer H_2O begins to dehydrate from Mg-Fe phyls (approximately 4 GPa, which corresponds to approximately 20 GPa in shock recovery experiments of CI/CY chondrites in figure 7a). Dehydration of adsorbed H_2O from Mg-Fe phyls and carbonaceous materials is

probably responsible for the amorphous material with a froth. Alternatively, localized high-temperature regions may have formed, causing only the Mg-Fe phyls to undergo vitrification or melting, as suggested by the similarity in chemical composition between the frothy regions and the original Mg-Fe phyls (Fig. 9c).

The frothy regions found in the shocked CI/CY chondrites (Fig. 1, 2, 3, 4, 9a, 9b) are not only amorphous and contain froths, but also tend to be enriched in iron compared to the Mg-Fe phyls in the host rock. As shown in Figure 9d, this compositional feature is similar to that of space weathered layers. Space weathering layers are formed not only by cosmic rays but also particle impacts (Noguchi et al., 2023). In this layer, Mg-Fe phyls, iron oxides, and FeS have become amorphous or melted. There are many similarities between the frothy regions formed by impact and those formed by space weathering in petrologic texture, constituents, and chemical composition. In the future, when frothy regions are discovered in Ryugu regolith grains and CI/CY chondrites, it will be necessary to investigate them carefully to determine whether they resulted from impact or space weathering.

4.5 Impacts on asteroid Ryugu

Most Ryugu grains so far studied exhibit no significant evidence of strong shock metamorphism (Ito et al., 2022; Nakamura et al., 2022; Nakamura et al., 2023; this study). Shock pressures experienced by some Ryugu grains have been estimated as follows: C0014, ~2 GPa (Tomioka et al., 2023), C0105-042, < ~4.5 GPa (Miyahara et al., 2024), A0104, >~4 GPa (Tomioka et al., 2024), A0304, ~0 GPa, C0230, ~0 GPa, and C0055, ~0–2 GPa (this study). Most of these estimated shock pressures are below approximately 4 GPa, at which fragmentation of rock along subparallel cracks is thought to begin due to dehydration and degassing of Mg-Fe phyls and carbonaceous materials. This implies that the Ryugu grains recovered by the HAYABUSA2 spacecraft are primarily rock fragments that were shattered by tensile fracturing during impacts.

The shock pressure at which fragmentation of rock along cracks (~4 GPa) or melting (~10 GPa) occurs in the CI/CY chondrites upon impact is already known. Based on this information, it may be possible to estimate the minimum impact velocity at which rock along cracks or melting begins using the Rankine-Hugoniot relationship. The shock pressure (P) on the surface of asteroid Ryugu can be expressed as follows:

$$P = \rho_0 Vp U \qquad \text{eq. (3)}$$

where ρ_0, Vp, and U are the density before impact, particle velocity, and shock wave velocity, respectively. We assumed the initial average bulk density of Ryugu grains: ρ_0 = 1.79 kg/m^3 (Nakamura et al., 2023). The relationship between the shock wave velocity (U) and the particle velocity (Vp) can be expressed by the following equation:

554 $$U = c_0 + sVp \qquad \text{eq (4)}$$
555 where c_0 and s are the bulk sound velocity and the dimensionless parameter depending
556 on the material, respectively. Assuming that the meteoroid hitting the asteroid Ryugu
557 and Ryugu are of the same material, the particle velocity (Vp) can be expressed by the
558 following equation:
559 $$Vp \approx Vi/2 \qquad \text{eq (5)}$$
560 where Vi is the impact velocity. We used the Hugoniot data for Murchison CM2 as a
561 simulant for CI/CY chondrites and calculated the shock pressures assuming c_0 = 1.87
562 km/s, s = 1.48 (Anderson and Ahrens, 1998). For shock pressures of 4 GPa and 10
563 GPa, the estimated impact velocities are ~1.5 km/s and ~2.8 km/s, respectively.
564 The estimated impact velocities are much slower than the most probable
565 impact velocity (~4.4 km/s) of meteoroids derived from asteroidal sources striking an
566 asteroid in the main belt (Bottke et al., 1994). Shock waves generated at the point of
567 impact propagate out in concentric circles, and when they reach the free surface away
568 from the impact point, they tear apart the rock, a process known as spallation. On
569 asteroid Ryugu, the spallation process would be significantly enhanced at shock
570 pressures above ~4 GPa due to the expansion force generated by the dehydration of
571 Mg-Fe phyls and the degassing of CO_2 from carbonaceous materials. Hence, the body
572 would be easily demolished even by weak shock metamorphism (Scott et al., 1992;
573 Tomeoka et al., 2003).
574 The collapse of C-type asteroids under weak shock pressure is also supported
575 by studies of CI/CY chondrites. Numerous petrological descriptions of CI/CY
576 chondrites have been made (Bischoff, 1998; Gounelle and Zolensky, 2014; King et al.,
577 2019; Tomeoka and Buseck, 1988). Dense subparallel cracks and melts that formed,
578 when the CI/CY chondrites were subjected to shock pressures above ~4 or ~10 GPa,
579 have not been reported. Nevertheless, near the impact point, shock pressures exceeding
580 10 GPa, which induce melting of CI/CY chondrites, are likely to occur (Nakamura et
581 al., 2023).
582 Some of the melted chondrite material may be ejected and solidified rapidly.
583 A trace amount of possible shock-induced melts has been identified in the Orgueil CI
584 chondrite (Zolensky et al., 2022). Regions that recorded high shock pressures and
585 temperatures may exist as "hot spots" beneath the regolith layer of asteroid Ryugu. If
586 such "hot spots" exist, they suggest that highly shocked materials could be retained
587 within the asteroid's interior and potentially provide valuable information of past
588 impacts and thermal events that the asteroid experienced. Further investigations,
589 including in-depth petrological and geochemical analyses of Ryugu samples, will be
590 essential to elucidate the nature and extent of these high-pressure, high-temperature

regions and their implications for the asteroid's evolutionary history.

5. Conclusions

a) Shock recovery experiments using CI/CY chondrites were successfully performed over a pressure range of approximately 5 to 40 GPa. To estimate equivalent shock pressures under natural impact conditions, the experimental values were adjusted based on waste heat energy considerations. This correction accounts for the difference in shock pressure development between natural impacts, which typically involve a single shock compression wave, and laboratory experiments, where shock compression waves may undergo multiple reflections.

b) Following the shock experiments, CI/CY chondrites exhibited various shock metamorphic textures, including matrix compression, the formation of subparallel cracks, and melting or vitrification. After applying the shock pressure correction to account for natural impact conditions, it is inferred that dehydration and degassing of Mg-Fe phyls and carbonaceous materials become significant at pressures exceeding approximately 4 GPa. These induce rock fragmentation along cracks due to the expansion pressure of volatile components. In contrast, extensive rock melting is not initiated until shock pressures exceed approximately 10 GPa.

c) Shock pressures below approximately 4 GPa are insufficient to produce pronounced shock metamorphic features, such as dense fracturing or melting. Although several Ryugu grains that potentially record shock metamorphism were examined in this and previous studies, no significant shock-related textures—such as closely spaced subparallel cracks or melt veins—have been observed. These observations support the interpretation that the majority of Ryugu grains were subjected to shock pressures lower than approximately 4 GPa.

d) Considering the typical impact velocities of meteoroids originating from asteroidal sources within the main belt, surface rock fragmentation along cracks on C-type asteroids is likely a frequent occurrence due to impacts. As a result, the regolith layer of asteroid Ryugu was formed through the reassembly of exfoliated rock fragments, rather than undergoing strong shock metamorphism.

Acknowledgments

Kazushige Tomeoka and an anonymous reviewer are acknowledged for their helpful comments that improved this manuscript. This study was conducted by the approval of the Ryugu Sample 2nd AO project: *The Estimation of Shock Metamorphism in Ryugu Grains Based on Shock Experiments of CI Chondrite (PI: T. Nakahashi)*. This study was partly supported by a Grant-in-Aid for Scientific Research,

no. 18H01269 from the Ministry of Education, Culture Sports, Science, and Technology (MEXT) to M.M. This study was also financially supported by NIPR through General Collaboration Projects number G6-14. This work was supported in part by World Premier International Research Center Initiative (WPI－MANA:NIMS) and NIMS Joint Research Hub Program.

References

Akai J. (1992) TTT diagram of serpentine and saponite, and estimation of metamorphic heating degree of Antarctic carbonaceous chondrites. In *Sixteenth Symposium on Antarctic Meteorites*, pp. 120–135, Itabashi, Tokyo.

Anderson W. W. and Ahrens T. J. (1998) Shock wave equations of state of chondritic meteorites. In *AIP Conference Proceedings*, pp. 115–118. American Institute of Physics, Amherst, Massachusetts.

Ball M. C. and Taylor H. F. W. (1963) The dehydration of chrysotile in air and under hydrothermal conditions. *Mineralogical Magazine and Journal of the Mineralogical Society* **33**, 467–482.

Bischoff A. (1998) Aqueous alteration of carbonaceous chondrites: Evidence for preaccretionary alteration—A review. *Meteoritics & Planetary Science* **33**, 1113–1122.

Bottke W. F., Nolan M. C., Greenberg R., and Kolvoord R. A. (1994) Velocity distributions among colliding asteroids. *Icarus* **107**, 255–268.

Braukmüller N., Wombacher F., Hezel D. C., Escoube R., and Münker C. (2018) The chemical composition of carbonaceous chondrites: Implications for volatile element depletion, complementarity and alteration. *Geochimica et Cosmochimica Acta* **239**, 17–48.

Brindley G. W. and Hayami R. (1963) Kinetics and mechanisms of dehydration and recrystallization of serpentine—I. *Clays and Clay Minerals* **12**, 35–47.

Bus S. J. and Binzel R. P. (2002) Phase II of the Small Main-Belt Asteroid Spectroscopic Survey: The Observations. *Icarus* **158**, 106–145.

Cattaneo A., Gualtieri A. F., and Artioli G. (2003) Kinetic study of the dehydroxylation of chrysotile asbestos with temperature by in situ XRPD. *Physics and Chemistry of Minerals* **30**, 177–183.

Ebihara M., Shirai N., Osawa T., and Yamaguchi A. (2025) Chemical characteristics of the Yamato-type (CY) carbonaceous chondrites. *Geochimica et Cosmochimica Acta* **389**, 200–210.

Francioso O., Montecchio D., Gioacchini P., and Ciavatta C. (2005) Thermal analysis (TG–DTA) and isotopic characterization (13C–15N) of humic acids from different origins. *Applied Geochemistry* **20**, 537–544.

Furukawa Y., Sekine T., Oba M., Kakegawa T., and Nakazawa H. (2009) Biomolecule formation by oceanic impacts on early Earth. *Nature Geoscience* **2**, 62–66.

Gounelle M. and Zolensky M. E. (2014) The Orgueil meteorite: 150 years of history. *Meteoritics & Planetary Science* **49**, 1769–1794.

Horie Y. and Sawaoka A. B. (1993) *Shock compression chemistry of materials*. KTK Scientific, Tokyo.

pp. 364.

Hu J. and Sharp T. G. (2022) Formation, preservation and extinction of high-pressure minerals in meteorites: temperature effects in shock metamorphism and shock classification. *Progress in Earth and Planetary Science* **9**, 6.

Ikeda Y. (1992) An overview of the research consortium," Antarctic carbonaceous chondrites with CI affinities, Yamato-86720, Yamato-82162, and Belgica-7904". *Antarctic Meteorite Research* **5**, 49–73.

Ito M., Tomioka N., Uesugi M., Yamaguchi A., Shirai N., Ohigashi T., Liu M.-C., Greenwood R. C., Kimura M., Imae N., Uesugi K., Nakato A., Yogata K., Yuzawa H., Kodama Y., Tsuchiyama A., Yasutake M., Findlay R., Franchi I. A., Malley J. A., McCain K. A., Matsuda N., McKeegan K. D., Hirahara K., Takeuchi A., Sekimoto S., Sakurai I., Okada I., Karouji Y., Arakawa M., Fujii A., Fujimoto M., Hayakawa M., Hirata N., Hirata N., Honda R., Honda C., Hosoda S., Iijima Y.-i., Ikeda H., Ishiguro M., Ishihara Y., Iwata T., Kawahara K., Kikuchi S., Kitazato K., Matsumoto K., Matsuoka M., Michikami T., Mimasu Y., Miura A., Mori O., Morota T., Nakazawa S., Namiki N., Noda H., Noguchi R., Ogawa N., Ogawa K., Okada T., Okamoto C., Ono G., Ozaki M., Saiki T., Sakatani N., Sawada H., Senshu H., Shimaki Y., Shirai K., Sugita S., Takei Y., Takeuchi H., Tanaka S., Tatsumi E., Terui F., Tsukizaki R., Wada K., Yamada M., Yamada T., Yamamoto Y., Yano H., Yokota Y., Yoshihara K., Yoshikawa M., Yoshikawa K., Fukai R., Furuya S., Hatakeda K., Hayashi T., Hitomi Y., Kumagai K., Miyazaki A., Nishimura M., Soejima H., Iwamae A., Yamamoto D., Yoshitake M., Yada T., Abe M., Usui T., Watanabe S.-i., and Tsuda Y. (2022) A pristine record of outer solar system materials from asteroid Ryugu's returned sample. *Nature Astronomy* **6**, 1163–1171.

Jaeger J. C., Cook N. G., and Zimmerman R. (2009) *Fundamentals of Rock Mechanics, 4th Edition*. Wiley-Blackwell, Hoboken. pp. 488.

Kieffer S. W. (1971) Shock metamorphism of the Coconino sandstone at meteor crater, Arizona. *Journal of Geophysical Research* **76**, 5449–5473.

Kieffer S. W. (1975) From regolith to rock by shock. *The moon* **13**, 301–320.

King A. J., Bates H. C., Krietsch D., Busemann H., Clay P. L., Schofield P. F., and Russell S. S. (2019) The Yamato-type (CY) carbonaceous chondrite group: Analogues for the surface of asteroid Ryugu? *Geochemistry* **79**, 125531.

King A. J., Solomon J. R., Schofield P. F., and Russell S. S. (2015) Characterising the CI and CI-like carbonaceous chondrites using thermogravimetric analysis and infrared spectroscopy. *Earth, Planets and Space* **67**, 198.

Knudson M. D., Hanson D. L., Bailey J. E., Hall C. A., Asay J. R., and Deeney C. (2004) Principal Hugoniot, reverberating wave, and mechanical reshock measurements of liquid deuterium to 400 GPa using plate impact techniques. *Physical Review B* **69**, 144209.

Kondo K., Sawaoka A., and Saito S. (1977) Magnetoflyer method for measuring gas-gun projectile

velocities. *Review of Scientific Instruments* **48**, 1581–1582.

Macke R. J., Consolmagno G. J., and Britt D. T. (2011) Density, porosity, and magnetic susceptibility of carbonaceous chondrites. *Meteoritics & Planetary Science* **46**, 1842–1862.

Marsh S. P. (1980) *LASL shock Hugoniot data*. University of California Press, Berkeley.

Miyahara M., Edanaga J., Yamaguchi A., Kobayashi T., Sekine T., and Nakamura A. (2021) Chondrule flattening by shock recovery experiments on unequilibrated chondrites. *Journal of Geophysical Research: Planets* **126**, e2021JE006864.

Miyahara M., Noguchi T., Matsumoto T., Tomioka N., Miyake A., Igami Y., Seto Y., Haruta M., Saito H., Hata S., Ishii H. A., Bradley J. P., Ohtaki K. K., Dobrică E., Leroux H., Le Guillou C., Jacob D., de la Peña F., Laforet S., Mouloud B.-E., Marinova M., Langenhorst F., Harries D., Beck P., Phan T. H. V., Rebois R., Abreu N. M., Gray J., Zega T., Zanetta P.-M., Thompson M. S., Stroud R., Burgess K., Cymes B. A., Bridges J. C., Hicks L., Lee M. R., Daly L., Bland P. A., Zolensky M. E., Frank D. R., Martinez J., Tsuchiyama A., Yasutake M., Matsuno J., Okumura S., Mitsukawa I., Uesugi K., Uesugi M., Takeuchi A., Sun M., Enju S., Takigawa A., Michikami T., Nakamura T., Matsumoto M., Nakauchi Y., Abe M., Nakazawa S., Okada T., Saiki T., Tanaka S., Terui F., Yoshikawa M., Miyazaki A., Nakato A., Nishimura M., Usui T., Yada T., Yurimoto H., Nagashima K., Kawasaki N., Sakamotoa N., Okazaki R., Yabuta H., Naraoka H., Sakamoto K., Tachibana S., Watanabe S., and Tsuda Y. (2024) Microscopic slickenside as a record of weak shock metamorphism in the surface layer of asteroid Ryugu. *Meteoritics & Planetary Science* **59**, 3181–3192.

Morlok A., Koike C., Tomioka N., Mann I., and Tomeoka K. (2010) Mid-infrared spectra of the shocked Murchison CM chondrite: Comparison with astronomical observations of dust in debris disks. *Icarus* **207**, 45–53.

Nakamura E., Kobayashi K., Tanaka R., Kunihiro T., Kitagawa H., Potiszil C., Ota T., Sakaguchi C., Yamanaka M., Ratnayake D. M., Tripathi H., Kumar R., Avramescu M.-L., Tsuchida H., Yachi Y., Miura H., Abe M., Fukai R., Furuya S., Hatakeda K., Hayashi T., Hitomi Y., Kumagai K., Miyazaki A., Nakato A., Nishimura M., Okada T., Soejima H., Sugita S., Suzuki A., Usui T., Yada T., Yamamoto D., Yogata K., Yoshitake M., Arakawa M., Fujii A., Hayakawa M., Hirata N., Hirata N., Honda R., Honda C., Hosoda S., Iijima Y.-i., Ikeda H., Ishiguro M., Ishihara Y., Iwata T., Kawahara K., Kikuchi S., Kitazato K., Matsumoto K., Matsuoka M., Michikami T., Mimasu Y., Miura A., Morota T., Nakazawa S., Namiki N., Noda H., Noguchi R., Ogawa N., Ogawa K., Okamoto C., Ono G., Ozaki M., Saiki T., Sakatani N., Sawada H., Senshu H., Shimaki Y., Shirai K., Takei Y., Takeuchi H., Tanaka S., Tatsumi E., Terui F., Tsukizaki R., Wada K., Yamada M., Yamada T., Yamamoto Y., Yano H., Yokota Y., Yoshihara K., Yoshikawa M., Yoshikawa K., Fujimoto M., Watanabe S.-i., and Tsuda Y. (2022) On the origin and evolution of the asteroid Ryugu: A comprehensive geochemical perspective. *Proceedings of the Japan Academy, Series B* **98**, 227–282.

Nakamura T., Matsumoto M., Amano K., Enokido Y., Zolensky M. E., Mikouchi T., Genda H., Tanaka S., Zolotov M. Y., Kurosawa K., Wakita S., Hyodo R., Nagano H., Nakashima D., Takahashi Y., Fujioka Y., Kikuiri M., Kagawa E., Matsuoka M., Brearley A. J., Tsuchiyama A., Uesugi M., Matsuno J., Kimura Y., Sato M., Milliken R. E., Tatsumi E., Sugita S., Hiroi T., Kitazato K., Brownlee D., Joswiak D. J., Takahashi M., Ninomiya K., Takahashi T., Osawa T., Terada K., Brenker F. E., Tkalcec B. J., Vincze L., Brunetto R., Aleon-Toppani A., Chan Q. H. S., Roskosz M., Viennet J. C., Beck P., Alp E. E., Michikami T., Nagaashi Y., Tsuji T., Ino Y., Martinez J., Han J., Dolocan A., Bodnar R. J., Tanaka M., Yoshida H., Sugiyama K., King A. J., Fukushi K., Suga H., Yamashita S., Kawai T., Inoue K., Nakato A., Noguchi T., Vilas F., Hendrix A. R., Jaramillo-Correa C., Domingue D. L., Dominguez G., Gainsforth Z., Engrand C., Duprat J., Russell S. S., Bonato E., Ma C., Kawamoto T., Wada T., Watanabe S., Endo R., Enju S., Riu L., Rubino S., Tack P., Takeshita S., Takeichi Y., Takeuchi A., Takigawa A., Takir D., Tanigaki T., Taniguchi A., Tsukamoto K., Yagi T., Yamada S., Yamamoto K., Yamashita Y., Yasutake M., Uesugi K., Umegaki I., Chiu I., Ishizaki T., Okumura S., Palomba E., Pilorget C., Potin S. M., Alasli A., Anada S., Araki Y., Sakatani N., Schultz C., Sekizawa O., Sitzman S. D., Sugiura K., Sun M., Dartois E., De Pauw E., Dionnet Z., Djouadi Z., Falkenberg G., Fujita R., Fukuma T., Gearba I. R., Hagiya K., Hu M. Y., Kato T., Kawamura T., Kimura M., Kubo M. K., Langenhorst F., Lantz C., Lavina B., Lindner M., Zhao J., Vekemans B., Baklouti D., Bazi B., Borondics F., Nagasawa S., Nishiyama G., Nitta K., Mathurin J., Matsumoto T., Mitsukawa I., Miura H., Miyake A., Miyake Y., Yurimoto H., Okazaki R., Yabuta H., Naraoka H., Sakamoto K., Tachibana S., Connolly H. C., Jr., Lauretta D. S., Yoshitake M., Yoshikawa M., Yoshikawa K., Yoshihara K., Yokota Y., Yogata K., Yano H., Yamamoto Y., Yamamoto D., Yamada M., Yamada T., Yada T., Wada K., Usui T., Tsukizaki R., Terui F., Takeuchi H., Takei Y., Iwamae A., Soejima H., Shirai K., Shimaki Y., Senshu H., Sawada H., Saiki T., Ozaki M., Ono G., Okada T., Ogawa N., Ogawa K., Noguchi R., Noda H., Nishimura M., Namiki N., Nakazawa S., Morota T., Miyazaki A., Miura A., Mimasu Y., Matsumoto K., Kumagai K., Kouyama T., Kikuchi S., Kawahara K., Kameda S., Iwata T., Ishihara Y., Ishiguro M., Ikeda H., Hosoda S., Honda R., Honda C., Hitomi Y., Hirata N., Hirata N., Hayashi T., Hayakawa M., Hatakeda K., Furuya S., Fukai R., Fujii A., Cho Y., Arakawa M., Abe M., Watanabe S., and Tsuda Y. (2023) Formation and evolution of carbonaceous asteroid Ryugu: Direct evidence from returned samples. *Science* **379**, eabn8671.

Nakamura T., Tomeoka K., Takaoka N., Sekine T., and Takeda H. (2000) Impact-induced textural changes of CV carbonaceous chondrites: Experimental reproduction. *Icarus* **146**, 289–300.

Noguchi T., Matsumoto T., Miyake A., Igami Y., Haruta M., Saito H., Hata S., Seto Y., Miyahara M., Tomioka N., Ishii H. A., Bradley J. P., Ohtaki K. K., Dobrică E., Leroux H., Le Guillou C., Jacob D., de la Peña F., Laforet S., Marinova M., Langenhorst F., Harries D., Beck P., Phan T. H. V., Rebois R., Abreu N. M., Gray J., Zega T., Zanetta P.-M., Thompson M. S., Stroud R.,

776 Burgess K., Cymes B. A., Bridges J. C., Hicks L., Lee M. R., Daly L., Bland P. A., Zolensky
777 M. E., Frank D. R., Martinez J., Tsuchiyama A., Yasutake M., Matsuno J., Okumura S.,
778 Mitsukawa I., Uesugi K., Uesugi M., Takeuchi A., Sun M., Enju S., Takigawa A., Michikami
779 T., Nakamura T., Matsumoto M., Nakauchi Y., Abe M., Arakawa M., Fujii A., Hayakawa M.,
780 Hirata N., Hirata N., Honda R., Honda C., Hosoda S., Iijima Y.-i., Ikeda H., Ishiguro M.,
781 Ishihara Y., Iwata T., Kawahara K., Kikuchi S., Kitazato K., Matsumoto K., Matsuoka M.,
782 Mimasu Y., Miura A., Morota T., Nakazawa S., Namiki N., Noda H., Noguchi R., Ogawa N.,
783 Ogawa K., Okada T., Okamoto C., Ono G., Ozaki M., Saiki T., Sakatani N., Sawada H., Senshu
784 H., Shimaki Y., Shirai K., Sugita S., Takei Y., Takeuchi H., Tanaka S., Tatsumi E., Terui F.,
785 Tsukizaki R., Wada K., Yamada M., Yamada T., Yamamoto Y., Yano H., Yokota Y., Yoshihara
786 K., Yoshikawa M., Yoshikawa K., Fukai R., Furuya S., Hatakeda K., Hayashi T., Hitomi Y.,
787 Kumagai K., Miyazaki A., Nakato A., Nishimura M., Soejima H., Suzuki A. I., Usui T., Yada
788 T., Yamamoto D., Yogata K., Yoshitake M., Connolly H. C., Lauretta D. S., Yurimoto H.,
789 Nagashima K., Kawasaki N., Sakamoto N., Okazaki R., Yabuta H., Naraoka H., Sakamoto K.,
790 Tachibana S., Watanabe S.-i., and Tsuda Y. (2023) A dehydrated space-weathered skin cloaking
791 the hydrated interior of Ryugu. *Nature Astronomy* **7**, 170–181.

792 Ohtani E., Sakurabayashi T., and Kurosawa K. (2022) Experimental simulations of shock textures in
793 BCC iron: implications for iron meteorites. *Progress in Earth and Planetary Science* **9**, 24.

794 Ono H., Kurosawa K., Niihara T., Mikouchi T., Tomioka N., Isa J., Kagi H., Matsuzaki T., Sakuma H.,
795 Genda H., Sakaiya T., Kondo T., Kayama M., Koike M., Sano Y., Murayama M., Satake W.,
796 and Matsui T. (2023) Experimentally Shock-Induced Melt Veins in Basalt: Improving the
797 Shock Classification of Eucrites. *Geophysical Research Letters* **50**, e2022GL101009.

798 Pohl L. and Britt D. T. (2020) Strengths of meteorites—An overview and analysis of available data.
799 *Meteoritics & Planetary Science* **55**, 962–987.

800 Presnall D. C., Weng Y.-H., Milholland C. S., and Walter M. J. (1998) Liquidus phase relations in the
801 system MgO–MgSiO3 at pressures up to 25 GPa—constraints on crystallization of a molten
802 Hadean mantle. *Physics of the Earth and Planetary Interiors* **107**, 83–95.

803 Scott E. R. D., Keil K., and Stöffler D. (1992) Shock metamorphism of carbonaceous chondrites.
804 *Geochimica et Cosmochimica Acta* **56**, 4281–4293.

805 Sekigawa C., Tomeoka K., and Seto Y. (2009) Fracture development in the experimentally shocked
806 Murchison CM chondrite: relationship between pressure and fracturing (in Japanese). In
807 *Annual Meeting of the Mineralogical Society of Japan 2009*, pp. R9-P01.

808 Stöffler D., Hamann C., and Metzler K. (2018) Shock metamorphism of planetary silicate rocks and
809 sediments: Proposal for an updated classification system. *Meteoritics & Planetary Science* **53**,
810 5–49.

811 Tachibana S., Sawada H., Okazaki R., Takano Y., Sakamoto K., Miura Y. N., Okamoto C., Yano H.,
812 Yamanouchi S., Michel P., Zhang Y., Schwartz S., Thuillet F., Yurimoto H., Nakamura T.,

Noguchi T., Yabuta H., Naraoka H., Tsuchiyama A., Imae N., Kurosawa K., Nakamura A. M., Ogawa K., Sugita S., Morota T., Honda R., Kameda S., Tatsumi E., Cho Y., Yoshioka K., Yokota Y., Hayakawa M., Matsuoka M., Sakatani N., Yamada M., Kouyama T., Suzuki H., Honda C., Yoshimitsu T., Kubota T., Demura H., Yada T., Nishimura M., Yogata K., Nakato A., Yoshitake M., Suzuki A. I., Furuya S., Hatakeda K., Miyazaki A., Kumagai K., Okada T., Abe M., Usui T., Ireland T. R., Fujimoto M., Yamada T., Arakawa M., Connolly H. C., Fujii A., Hasegawa S., Hirata N., Hirata N., Hirose C., Hosoda S., Iijima Y., Ikeda H., Ishiguro M., Ishihara Y., Iwata T., Kikuchi S., Kitazato K., Lauretta D. S., Libourel G., Marty B., Matsumoto K., Michikami T., Mimasu Y., Miura A., Mori O., Nakamura-Messenger K., Namiki N., Nguyen A. N., Nittler L. R., Noda H., Noguchi R., Ogawa N., Ono G., Ozaki M., Senshu H., Shimada T., Shimaki Y., Shirai K., Soldini S., Takahashi T., Takei Y., Takeuchi H., Tsukizaki R., Wada K., Yamamoto Y., Yoshikawa K., Yumoto K., Zolensky M. E., Nakazawa S., Terui F., Tanaka S., Saiki T., Yoshikawa M., Watanabe S., and Tsuda Y. (2022) Pebbles and sand on asteroid (162173) Ryugu: In situ observation and particles returned to Earth. *Science* **375**, 1011–1016.

Tomeoka K. and Buseck P. R. (1988) Matrix mineralogy of the Orgueil CI carbonaceous chondrite. *Geochimica et Cosmochimica Acta* **52**, 1627–1640.

Tomeoka K., Kiriyama K., Nakamura K., Yamahana Y., and Sekine T. (2003) Interplanetary dust from the explosive dispersal of hydrated asteroids by impacts. *Nature* **423**, 60–62.

Tomeoka K., Yamahana Y., and Sekine T. (1999) Experimental shock metamorphism of the Murchison CM carbonaceous chondrite. *Geochimica et Cosmochimica Acta* **63**, 3683–3703.

Tomioka N., Kurosawa K., Miyake A., Igami Y., Nagaya T., Noguchi T., Matsumoto T., Miyahara M., and Seto Y. (2024) Progressive change in dislocation microstructures in shocked calcite with pressure: Characterization of micrometeoroid bombardment on asteroid Ryugu. *American Mineralogist*.

Tomioka N. and Miyahara M. (2017) High-pressure minerals in shocked meteorites. *Meteoritics & Planetary Science* **52**, 2017–2039.

Tomioka N., Tomeoka K., Nakamura-Messenger K., and Sekine T. (2007) Heating effects of the matrix of experimentally shocked Murchison CM chondrite: Comparison with micrometeorites. *Meteoritics & Planetary Science* **42**, 19–30.

Tomioka N., Yamaguchi A., Ito M., Uesugi M., Imae N., Shirai N., Ohigashi T., Kimura M., Liu M.-C., Greenwood R. C., Uesugi K., Nakato A., Yogata K., Yuzawa H., Kodama Y., Hirahara K., Sakurai I., Okada I., Karouji Y., Okazaki K., Kurosawa K., Noguchi T., Miyake A., Miyahara M., Seto Y., Matsumoto T., Igami Y., Nakazawa S., Okada T., Saiki T., Tanaka S., Terui F., Yoshikawa M., Miyazaki A., Nishimura M., Yada T., Abe M., Usui T., Watanabe S.-i., and Tsuda Y. (2023) A history of mild shocks experienced by the regolith particles on hydrated asteroid Ryugu. *Nature Astronomy* **7**, 170–181.

Tsuchiyama A., Mashio E., Imai Y., Noguchi T., Miura Y. N., and Yano H. (2008) Strength measurements of carbonaceous chondrites and cosmic dust analogs using micro compression testing machine. In *Japan Geosciences Union Meeting, Abstracts of Papers*, pp. P168-002.

Wakita S., Genda H., Kurosawa K., Davison T. M., and Johnson B. C. (2022) Effect of Impact Velocity and Angle on Deformational Heating and Postimpact Temperature. *Journal of Geophysical Research: Planets* **127**, e2022JE007266.

Walker P. and Tarn W. H. (1990) *CRC handbook of metal etchants*. CRC press, Boca Raton.

Watanabe S., Hirabayashi M., Hirata N., Hirata N., Noguchi R., Shimaki Y., Ikeda H., Tatsumi E., Yoshikawa M., Kikuchi S., Yabuta H., Nakamura T., Tachibana S., Ishihara Y., Morota T., Kitazato K., Sakatani N., Matsumoto K., Wada K., Senshu H., Honda C., Michikami T., Takeuchi H., Kouyama T., Honda R., Kameda S., Fuse T., Miyamoto H., Komatsu G., Sugita S., Okada T., Namiki N., Arakawa M., Ishiguro M., Abe M., Gaskell R., Palmer E., Barnouin O. S., Michel P., French A. S., McMahon J. W., Scheeres D. J., Abell P. A., Yamamoto Y., Tanaka S., Shirai K., Matsuoka M., Yamada M., Yokota Y., Suzuki H., Yoshioka K., Cho Y., Tanaka S., Nishikawa N., Sugiyama T., Kikuchi H., Hemmi R., Yamaguchi T., Ogawa N., Ono G., Mimasu Y., Yoshikawa K., Takahashi T., Takei Y., Fujii A., Hirose C., Iwata T., Hayakawa M., Hosoda S., Mori O., Sawada H., Shimada T., Soldini S., Yano H., Tsukizaki R., Ozaki M., Iijima Y., Ogawa K., Fujimoto M., Ho T.-M., Moussi A., Jaumann R., Bibring J.-P., Krause C., Terui F., Saiki T., Nakazawa S., and Tsuda Y. (2019) Hayabusa2 arrives at the carbonaceous asteroid 162173 Ryugu-A spinning top-shaped rubble pile. *Science* **364**, 268–272.

Weber J. N. and Greer R. T. (1965) Dehydration of serpentine: heat of reaction and reaction kinetics at P_{H2O}=1 ATM. *American Mineralogist* **50**, 450–464.

Yamaguchi A., Tomioka N., Ito M., Shirai N., Kimura M., Greenwood R. C., Liu M.-C., McCain K. A., Matsuda N., Uesugi M., Imae N., Ohigashi T., Uesugi K., Nakato A., Yogata K., Yuzawa H., Kodama Y., Hirahara K., Sakurai I., Okada I., Karouji Y., Nakazawa S., Okada T., Saiki T., Tanaka S., Terui F., Yoshikawa M., Miyazaki A., Nishimura M., Yada T., Abe M., Usui T., Watanabe S.-i., and Tsuda Y. (2023) Insight into multi-step geological evolution of C-type asteroids from Ryugu particles. *Nature Astronomy* **7**, 398–405.

Yokoyama T., Nagashima K., Nakai I., Young E. D., Abe Y., Aléon J., Alexander C. M. O. D., Amari S., Amelin Y., Bajo K.-i., Bizzarro M., Bouvier A., Carlson R. W., Chaussidon M., Choi B.-G., Dauphas N., Davis A. M., Di Rocco T., Fujiya W., Fukai R., Gautam I., Haba M. K., Hibiya Y., Hidaka H., Homma H., Hoppe P., Huss G. R., Ichida K., Iizuka T., Ireland T. R., Ishikawa A., Ito M., Itoh S., Kawasaki N., Kita N. T., Kitajima K., Kleine T., Komatani S., Krot A. N., Liu M.-C., Masuda Y., McKeegan K. D., Morita M., Motomura K., Moynier F., Nguyen A., Nittler L., Onose M., Pack A., Park C., Piani L., Qin L., Russell S. S., Sakamoto N., Schönbächler M., Tafla L., Tang H., Terada K., Terada Y., Usui T., Wada S., Wadhwa M., Walker R. J., Yamashita K., Yin Q.-Z., Yoneda S., Yui H., Zhang A.-C., Connolly H. C.,

Lauretta D. S., Nakamura T., Naraoka H., Noguchi T., Okazaki R., Sakamoto K., Yabuta H., Abe M., Arakawa M., Fujii A., Hayakawa M., Hirata N., Hirata N., Honda R., Honda C., Hosoda S., Iijima Y.-i., Ikeda H., Ishiguro M., Ishihara Y., Iwata T., Kawahara K., Kikuchi S., Kitazato K., Matsumoto K., Matsuoka M., Michikami T., Mimasu Y., Miura A., Morota T., Nakazawa S., Namiki N., Noda H., Noguchi R., Ogawa N., Ogawa K., Okada T., Okamoto C., Ono G., Ozaki M., Saiki T., Sakatani N., Sawada H., Senshu H., Shimaki Y., Shirai K., Sugita S., Takei Y., Takeuchi H., Tanaka S., Tatsumi E., Terui F., Tsuda Y., Tsukizaki R., Wada K., Watanabe S.-i., Yamada M., Yamada T., Yamamoto Y., Yano H., Yokota Y., Yoshihara K., Yoshikawa M., Yoshikawa K., Furuya S., Hatakeda K., Hayashi T., Hitomi Y., Kumagai K., Miyazaki A., Nakato A., Nishimura M., Soejima H., Suzuki A., Yada T., Yamamoto D., Yogata K., Yoshitake M., Tachibana S., and Yurimoto H. (2023) Samples returned from the asteroid Ryugu are similar to Ivuna-type carbonaceous meteorites. *Science* **379**, eabn7850.

Zolensky M., Mikouchi T., Hagiya K., Ohsumi K., Komatsu M., Cheng A., and Le L. (2022) Evidence for impact shock and regolith transportation on CM, CI, and CV chondrite parent asteroids. *Meteoritics & Planetary Science* **57**, 1902–1919.

Figure captions

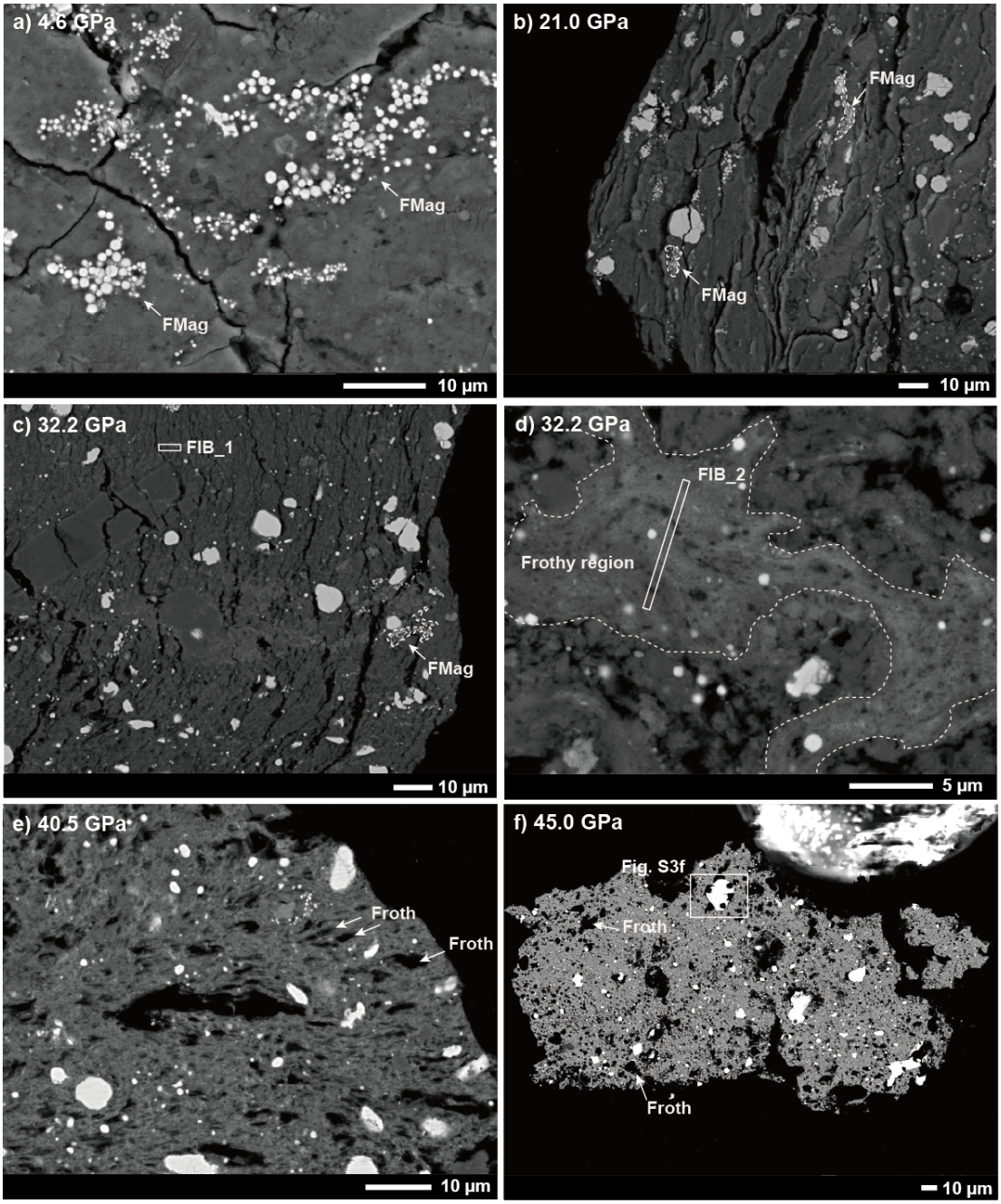

905

906 **Figure 1**. BSE images of Orgueil CI chondrite recovered from shock experiments. a)
907 Some FMgs exhibit deformation (Lower magnification image of this area is shown in
908 Figure S3a), b) Subparallel cracks are present (Lower magnification image of this area
909 is shown in Figure S3b). Deformed FMgs are outlined with dashed lines. c) Subparallel
910 cracks occur with high density. Deformed FMgs are outlined. d) A frothy region (white
911 dashed lines) occurs in some parts. e) All area is a frothy region. Many elongated froths
912 appear (white arrows). f) The original petrologic textures of the starting material have
913 been lost, giving way to the formation of a frothy region. A froth is indicated by white

arrows. The area of the FIB-excavated TEM foil is indicated by a numbered white box. FMg: framboidal magnetite cluster.

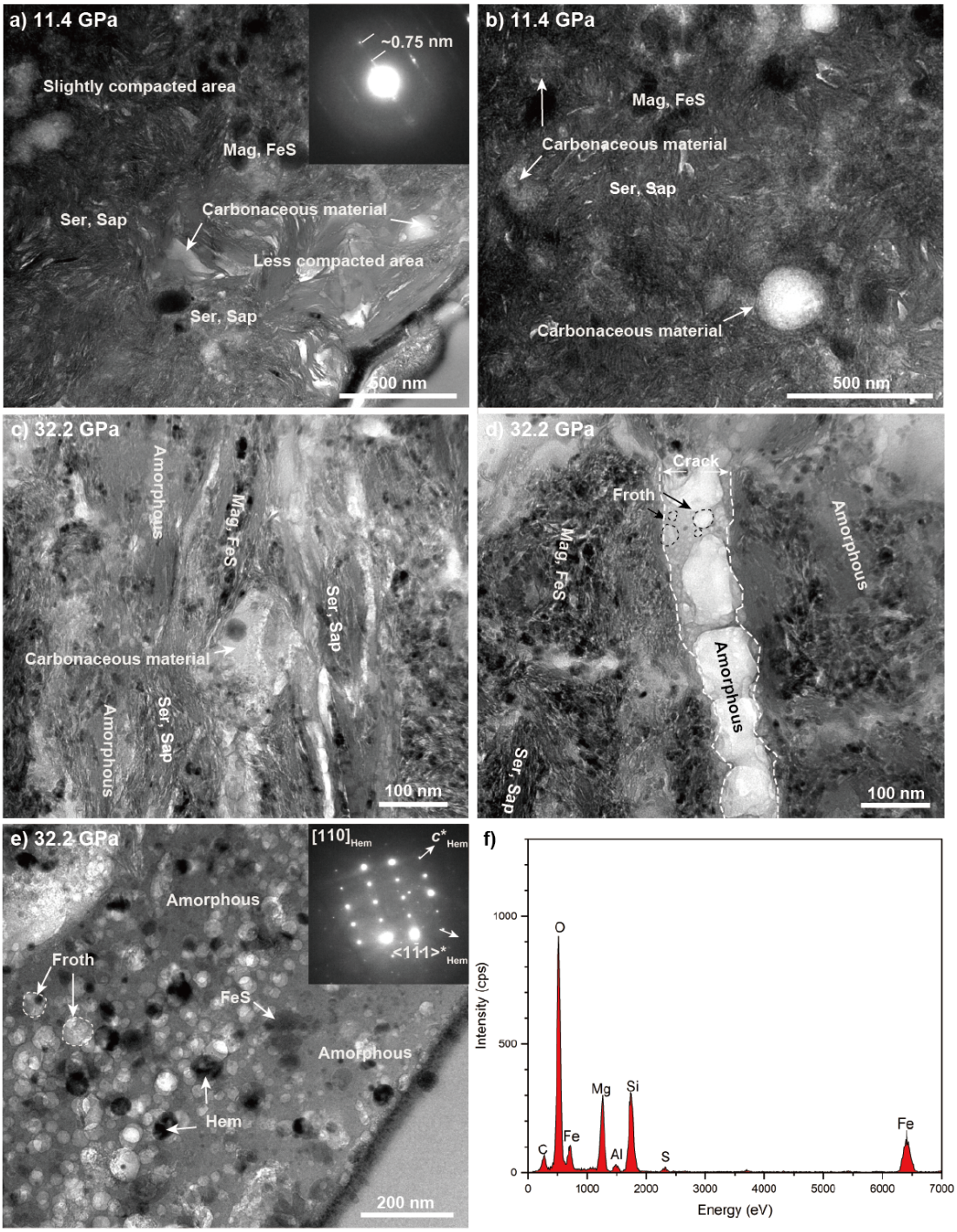

Figure 2. BF-TEM images of the Orgueil CI chondrite recovered from shock experiments. a) The matrix is slightly compacted in part (FIB_3 foil). The inset shows

the Selected Electron Diffraction (SAED) pattern corresponding to serpentine in the less compacted part. b) Even in the slightly compacted part, most of the micro/nano globules retain their spherical shape (FIB_3 foil). c) A region with densely spaced subparallel cracks (FIB_1 foil). d) The crack in the region is filled with an amorphous material (frothy region). e) Amorphous material, spherical hematite, FeS, and froth occur in the frothy region (FIB_2 foil). The inset shows the SAED pattern corresponding to hematite. f) Representative EDS spectrum obtained from the amorphous material within the frothy region shown in e). The locations of the FIB_1, FIB_2, and FIB_3 foils are shown in Figure 1c, Figure 1d, and Figure S3b, respectively. Sap: saponite, Ser: serpentine, Mag: magnetite, Hem: hematite, FeS: iron-sulfide.

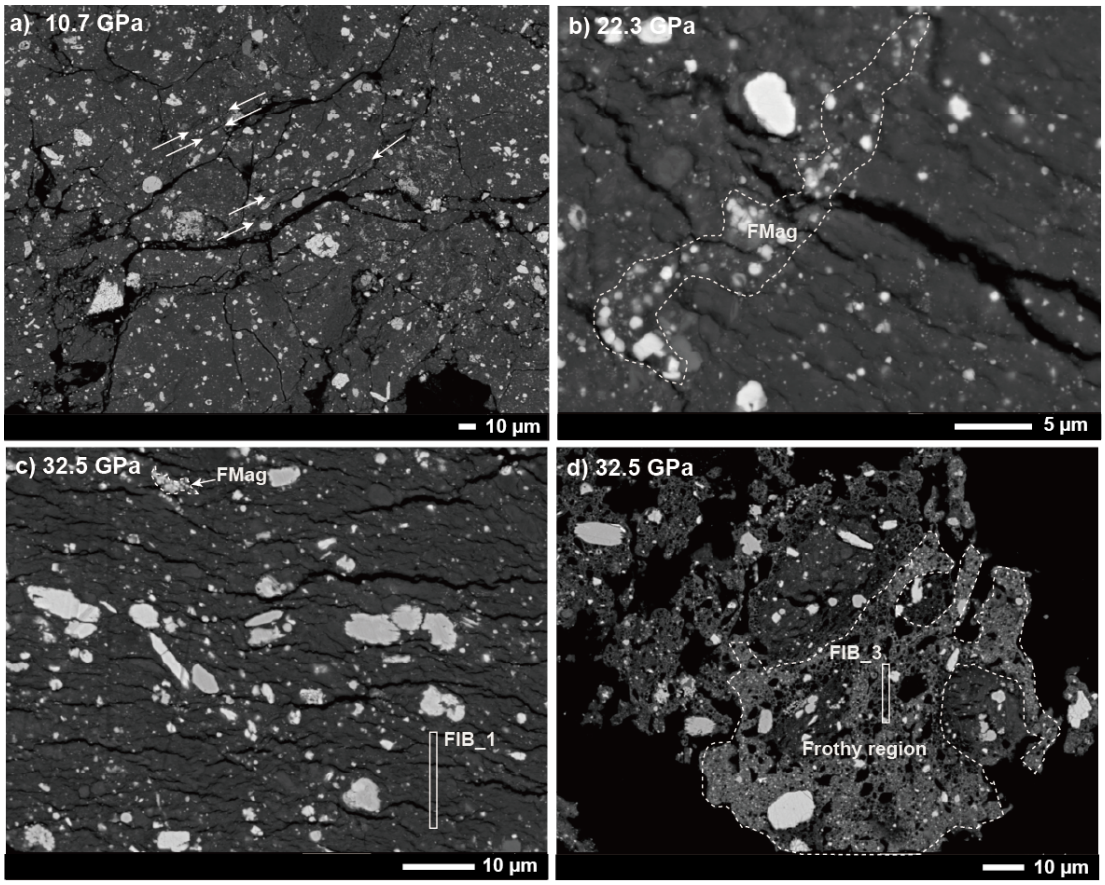

Figure 3. BSE images of Y 980115 CY chondrite recovered from shock experiments. a) Irregular cracks occur. A white arrow marks a short subparallel crack. b) Subparallel cracks occur. A deformed and dispersed FMg is outlined by dashed lines. c) Subparallel cracks occur at high density. A deformed FMg is outlined. d) A frothy region occurs in some parts. A froth region is outlined with a white dashed line. The FIB-excavated TEM foil is indicated by a numbered white box. FMg: framboidal magnetite cluster.

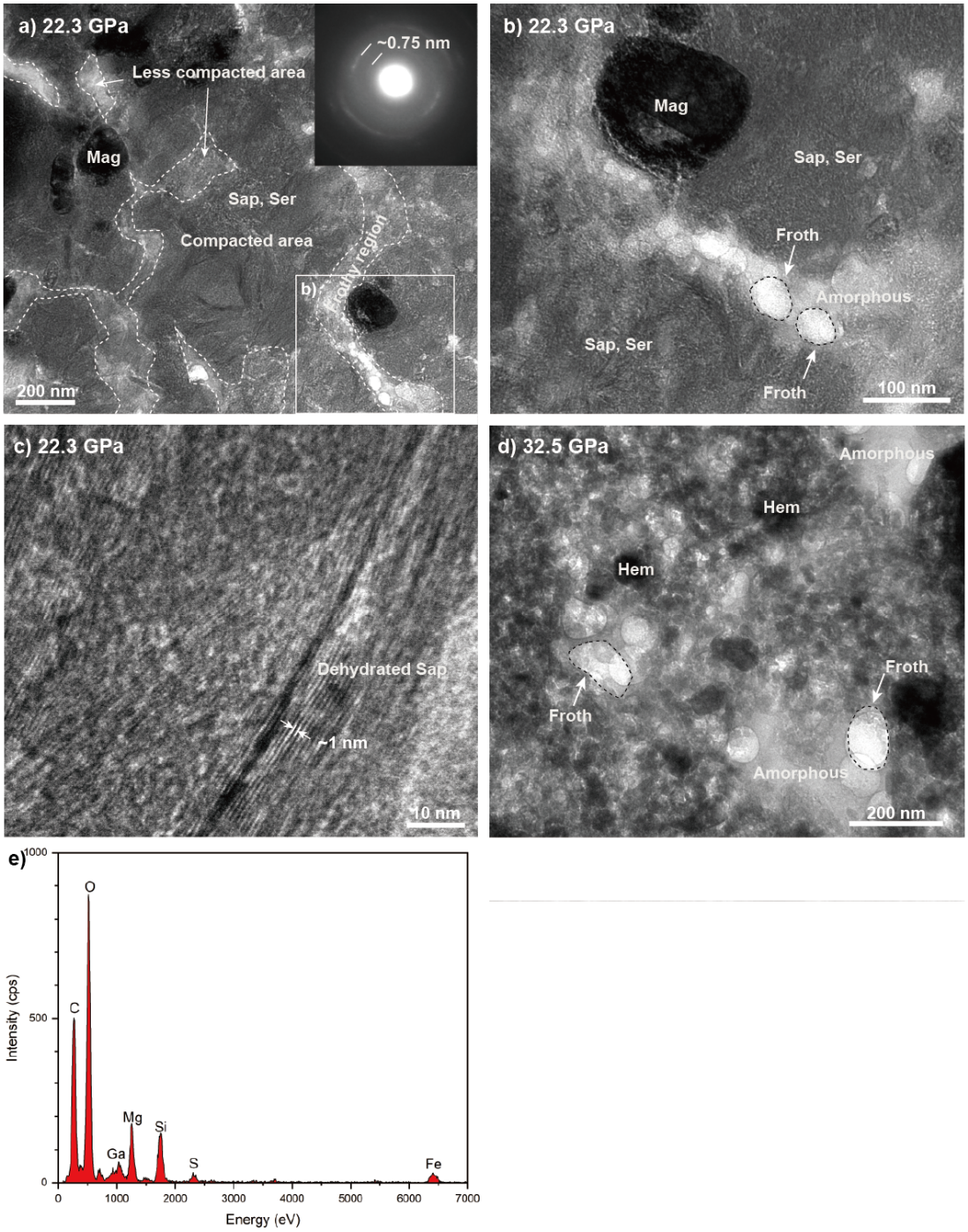

Figure 4. BF-TEM images of Y 980115 CY chondrite recovered from shock experiments. a) Saponite and serpentine packets are densely compacted and entangled, whereas localized regions exhibit loose compaction with remaining interstitial voids (FIB_2 foil). Subparallel cracks filled with a frothy region are present in the compacted portion. b) Magnified image of the white box in a). A froth is outlined with a black dashed line. c) Saponite survives without vitrification in some parts. d) Amorphous material and spherical hematite occur in the frothy region (FIB_3 foil). A froth is outlined with a black dashed line. e) Representative EDS spectrum taken from the

frothy region in d). The locations of the FIB_2 and FIB_3 foils are shown in Figure S4 and Figure 3d, respectively. Sap: saponite, Ser: serpentine, Mag: magnetite, Hem: hematite.

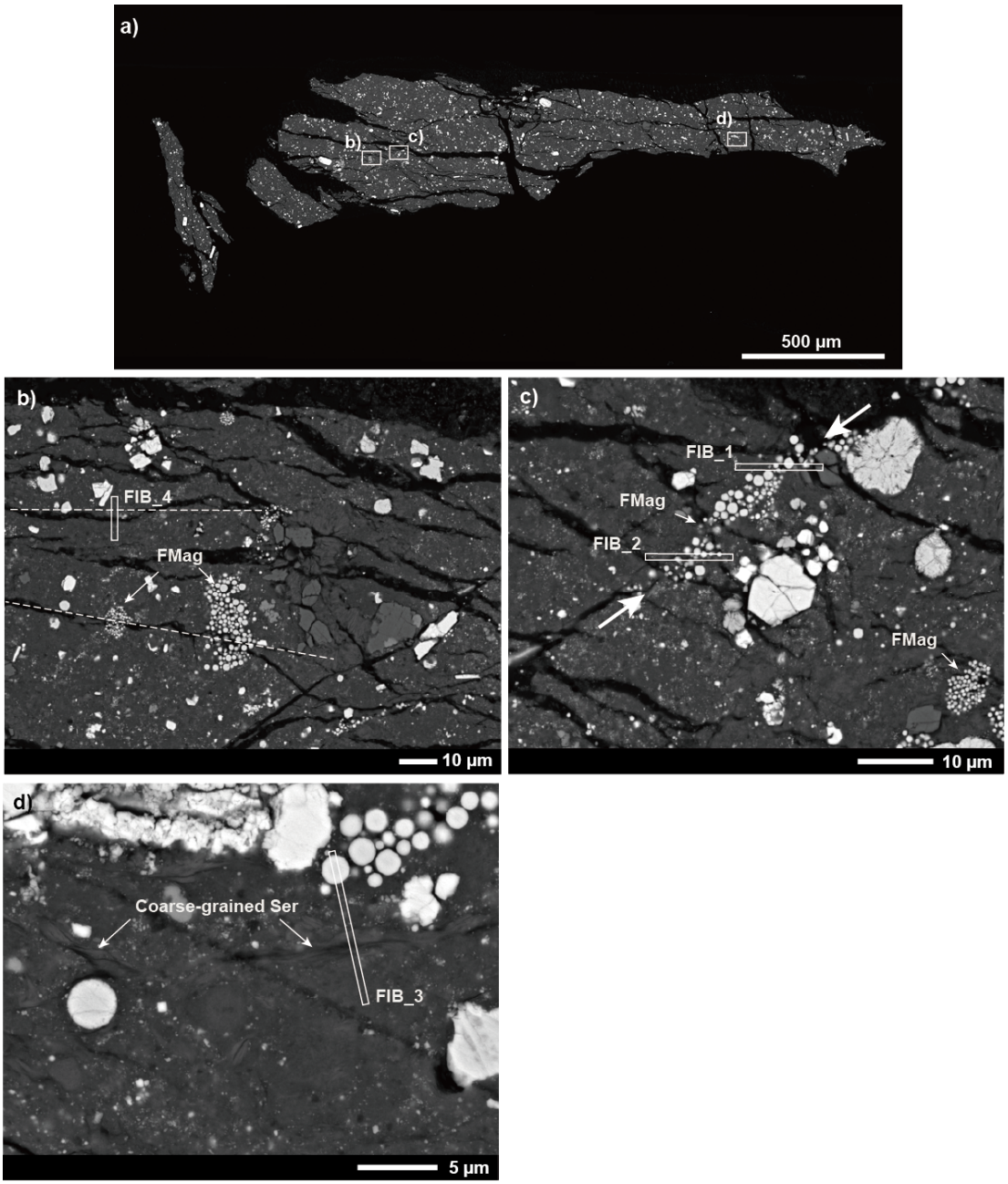

Figure 5. a) Whole area BSE image of C0055 Ryugu grain. b) Some FMgs intersect with subparallel cracks (dashed line). c) The FMg (between white arrows) is elongated along a crack oblique to the subparallel cracks. d) Some cracks are present along coarse-grained serpentine packets. The portions from where FIB-excavated TEM foils were prepared are indicated by numbered white boxes. FMg: framboidal magnetite cluster. Ser: serpentine.

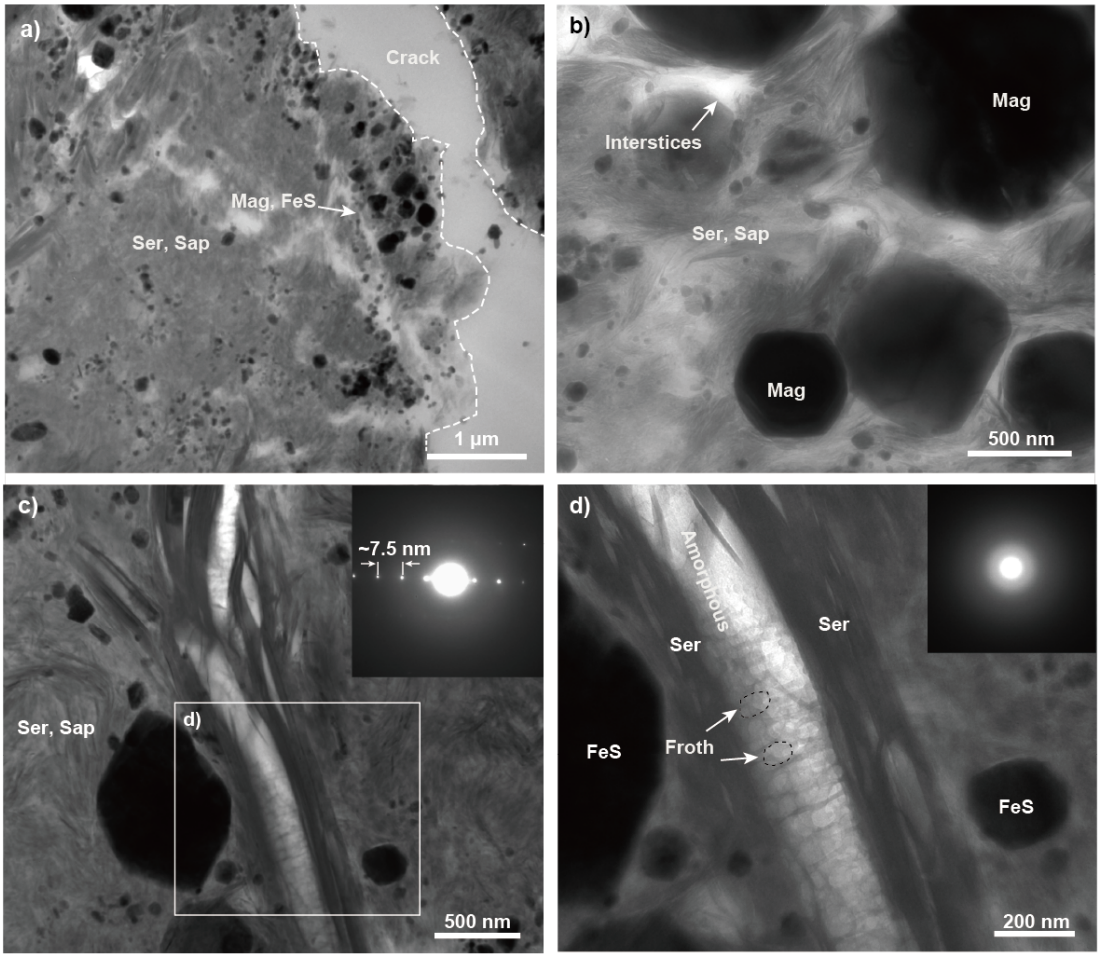

Figure 6. TEM images of C0055 Ryugu grain. a) The compacted matrix around a subparallel crack (FIB_4 foil). b) Heterogeneously compacted Mg-Fe phyls packets between magnetite grains existing a crack developing oblique to the subparallel cracks (FIB_2 foil). c) Coarse-grained Mg-Fe phyls packets (FIB_3 foil). d) Magnified image of the white box in c). The locations of the FIB_2, _3, and _4 foils are shown in Figure 5c, 5d, and 5b, respectively. Sap: saponite, Ser: serpentine, Mag: magnetite, Hem: hematite.

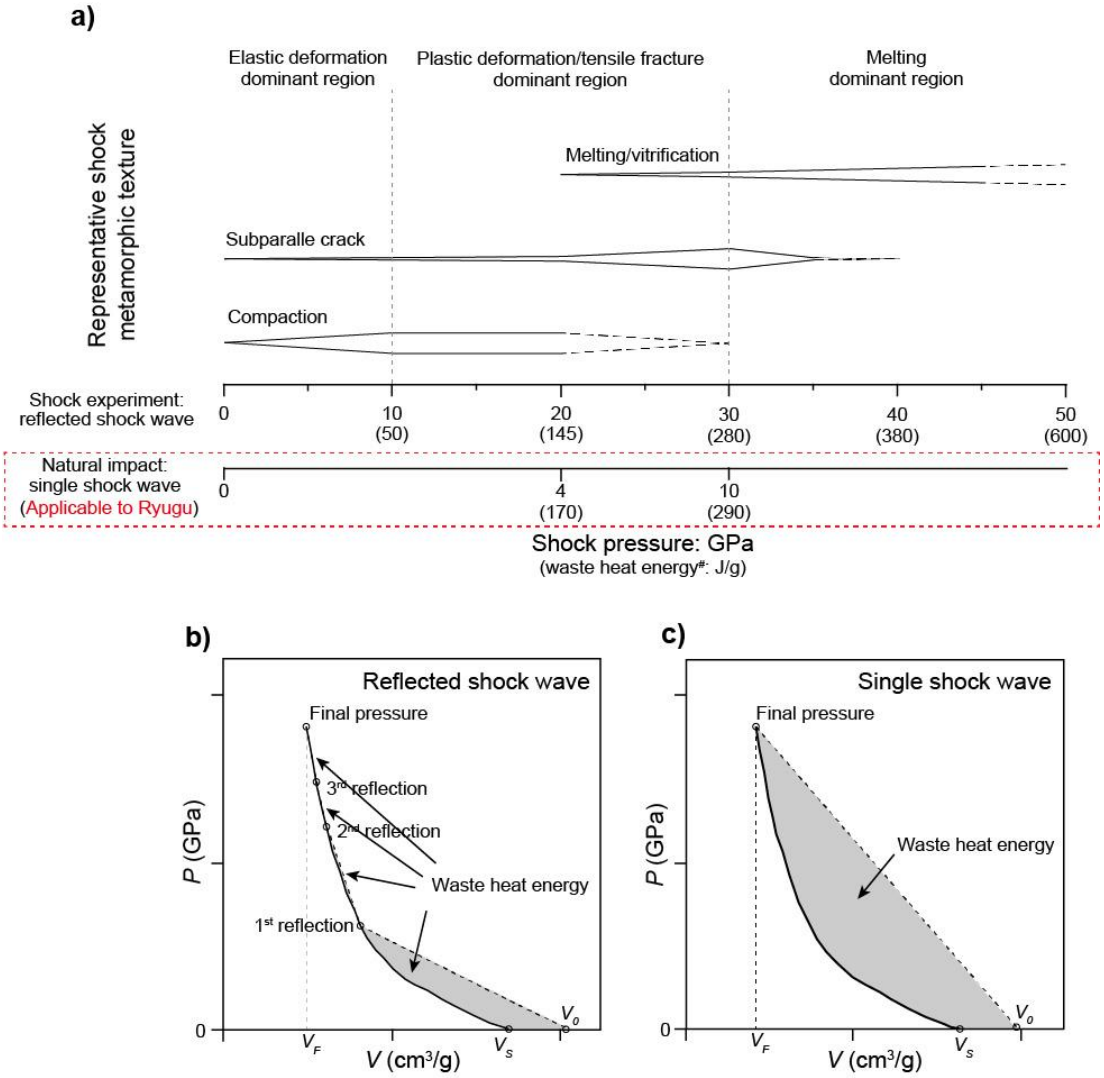

Figure 7. A schematic illustrating a) a representative shock metamorphic texture along with its corresponding shock pressure and the pressure (P)–volume (V) path for (b) a reflected shock wave and (c) a single shock wave, both reaching the same final shock pressure. In panel a), the horizontal axis presents both the shock pressure derived from shock recovery experiments and the estimated shock pressure for a natural impact event, which is inferred based on waste heat energy. In panel b), the shock loading path for shock experiments involving reflected shock waves, indicated by dashed lines, progresses from the initial volume (V_0) to the final pressure through a sequence of first, second, and third reflections. In panel c), the shock loading path for a natural impact event, also represented by dashed lines, follows a direct trajectory from V_0 to the final pressure. The solid lines in the diagram represent the path of adiabatic expansion, extending from V_S (the calculated volume of a nonporous sample) to the final pressure. The total amount of waste heat energy is depicted as the sum of the gray-shaded regions. V_0, the initial volume of the sample; V_F, the final volume of the sample; and

Vs, the calculated volume of the nonporous sample. The *P*-*V* path diagram is adapted from Tomeoka et al. (1999), and the values used for waste heat energy reference Tomeoka et al. (1999).

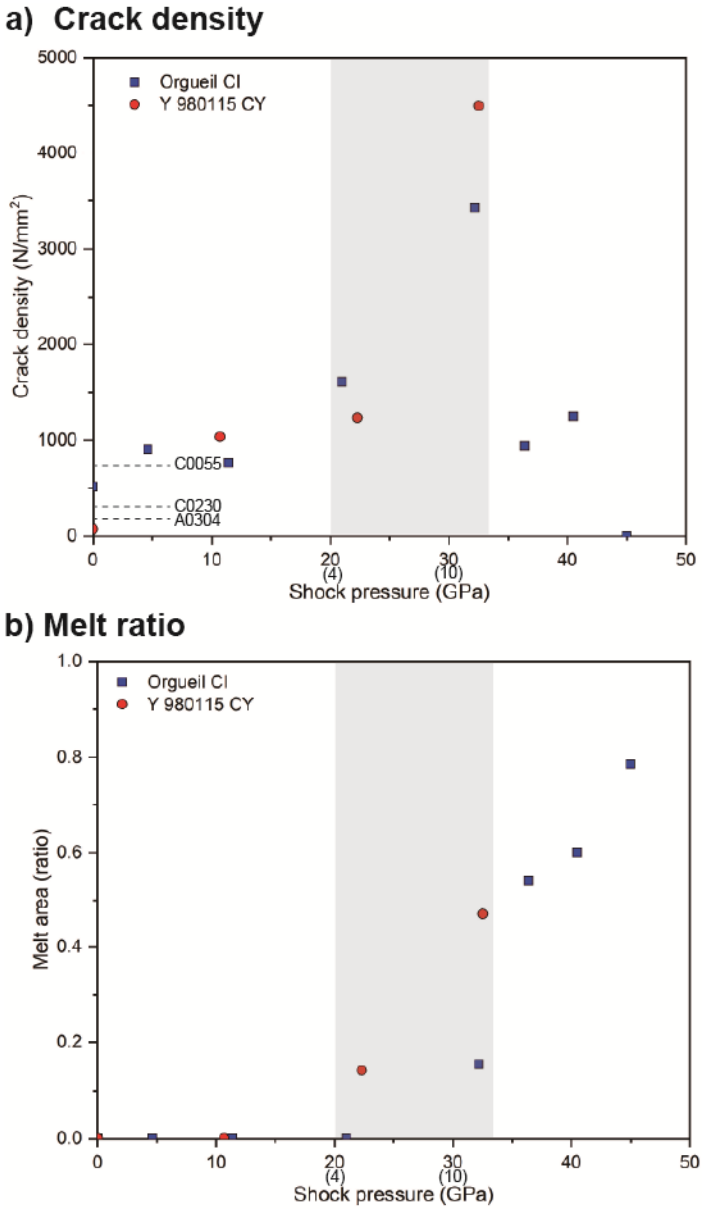

Figure 8. Relationships between shock pressure and a) crack density and b) melt ratio. Gray area: Area of extensive increase in crack density or melt ratio. The measured crack densities of the A0304, C0230, and C0055 Ryugu grains are indicated by dashed lines. The values in parentheses represent the estimated shock pressures for natural impact events, inferred based on waste heat energy (See the text and Figure 7a).

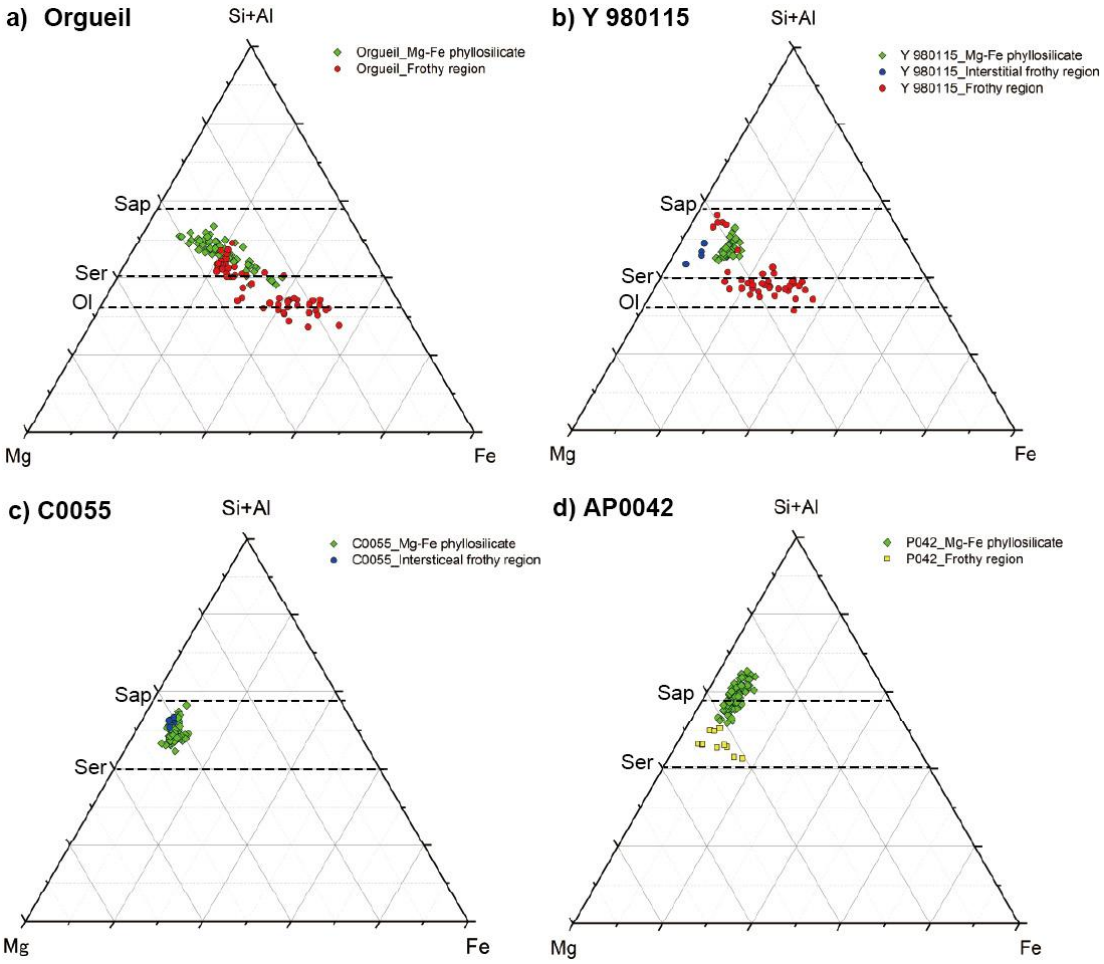

Figure 9. Si+Al–Mg–Fe ternary plots based on STEM–EDS analysis. Sap: saponite; Ser: serpentine; Ol: olivine. a, b) The Mg–Fe phyllosilicates in the starting materials are shown as green diamonds. Frothy regions are indicated by red circles, and interstitial frothy regions by blue circles; details are provided in the main text, c) The Mg–Fe phyllosilicates (green diamonds) correspond to the unaltered matrix of the C0055 Ryugu grain. Blue circles indicate interstitial frothy regions, as discussed in the main text. d) The frothy regions (yellow squares) observed in the AP0042 Ryugu grain are interpreted as a space weathering layer (Noguchi et al., 2023). The Mg–Fe phyllosilicates (green diamonds) represent the underlying unaltered matrix.

1006 Table 1. Run table for shock experiments.

run no.	sample				recovered sample	flyer	impact velocity (km/s)	equilibrium pressure (GPa)
	mass (g)	thickness (cm)	diameter (cm)	density (g/cm^3)[#2]	mass (g)			
Or_1	0.070	0.112	0.60	2.21	0.020	SUS304	0.58	11.4
Or_2	0.069	0.123	0.60	1.99	0.020	SUS304	1.00	21.0
Or_3	0.075	0.130	0.60	2.04	0.010	SUS304	1.44	32.2
Or_4	0.051	0.114	0.50	2.28	0.051	PE	1.22	4.6
Or_5	0.070	0.127	0.60	1.95	0.050	SUS304	1.54	36.4
Or_6	0.070	0.144	0.60	1.72	0.049	SUS304	1.72	40.5
Or_7	0.070	0.122	0.60	2.03	0.000	W	1.60	45.0
Y_1	0.080	0.160	0.60	1.77	0.046	SUS304	0.54	10.7
Y_2	0.090	0.160	0.60	1.99	0.035	SUS304	1.45	32.5
Y_3	0.079	0.160	0.60	1.75	0.011	SUS304	1.05	22.3
Y_4[#1]	0.085	0.160	0.60	1.88	-	SUS304	1.72	40.0

1007 Or: Orgueil CI, Y: Yamato 980115 CY, PE: polyethylene, W: tungsten, #1 The sample was not recovered, #2 The density was calculated from
1008 the mass and volume.
1009

Supporting materials

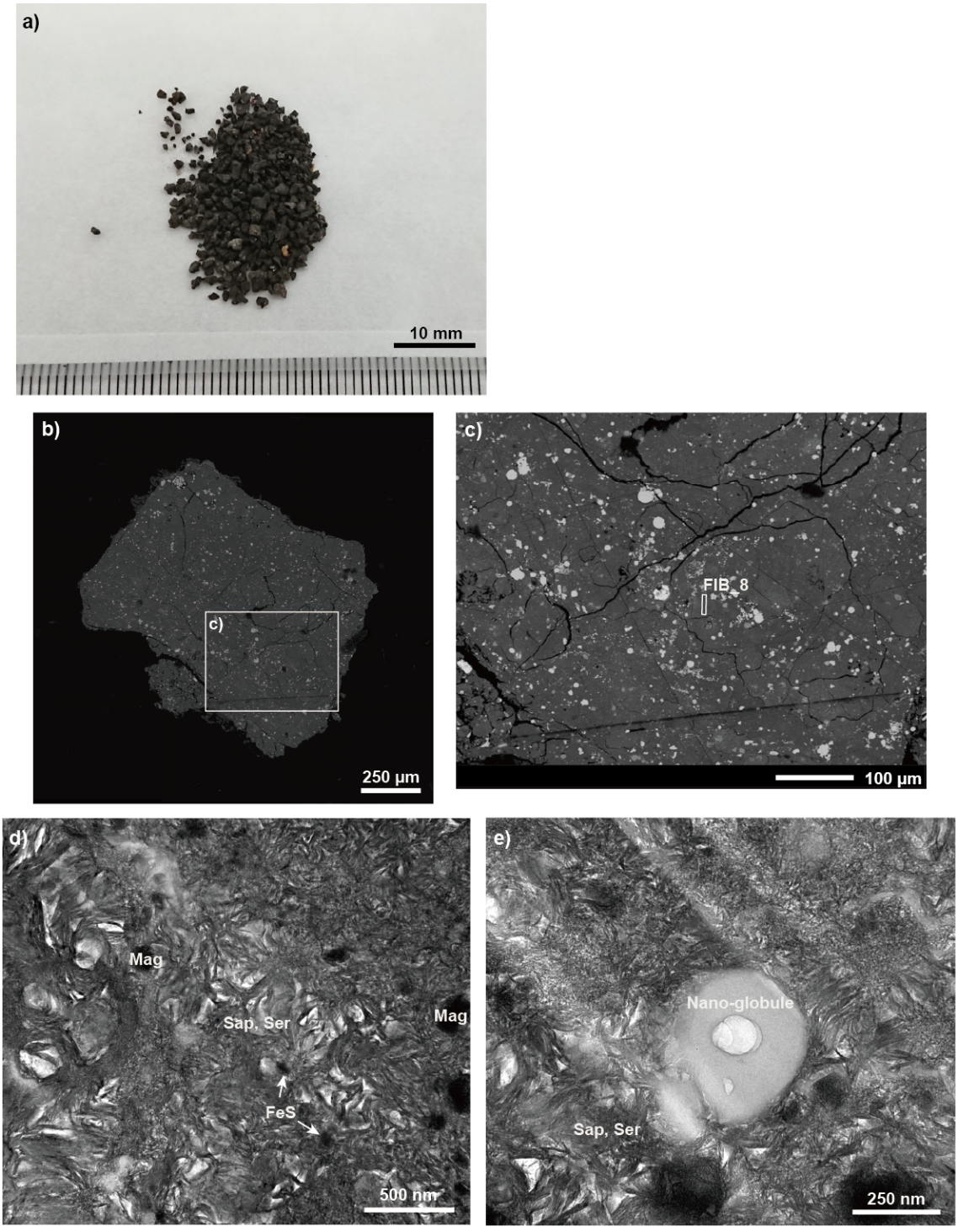

Figure S1. Orgueil CI chondrite (starting material). a) Orgueil granular sample, b) Low magnification back-scattered electron (BSE) image showing the typical fragment of Orgueil CI. c) Magnified image of a white box in b). The FIB-excavated TEM foil is

indicated by a numbered white box. d) and e) Bright-field (BF)-TEM images showing the typical matrix texture of Orgueil CI (FIB_8 foil). The black and white contrasts in the oblique direction are the FIB sputtering marks. Sap: saponite, Ser: serpentine, Mag: magnetite, FeS: iron sulfide.

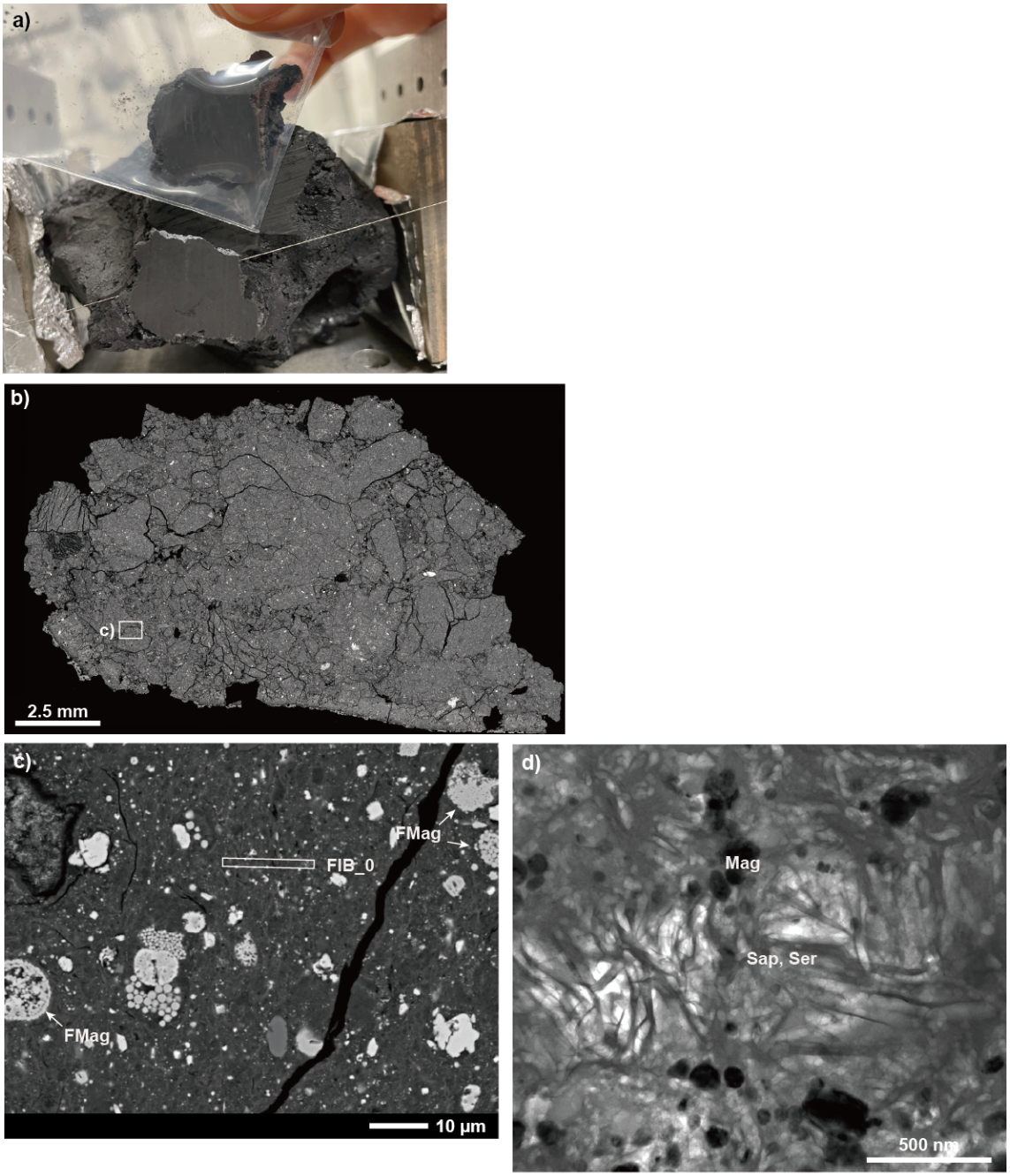

Figure S2. Y 980115 CY chondrite (starting material). a) Y 980115 slice sample after

cutting, b) Low magnification BSE image of Y 980115 CY. c) Magnified image of a white box in b). The FIB-excavated TEM foil is indicated by a numbered white box. d) BF-TEM image showing the typical matrix texture of Y 980115 CY (FIB_0 foil). Sap: saponite, Ser: serpentine, Mag: magnetite, FMg: framboidal magnetite cluster.

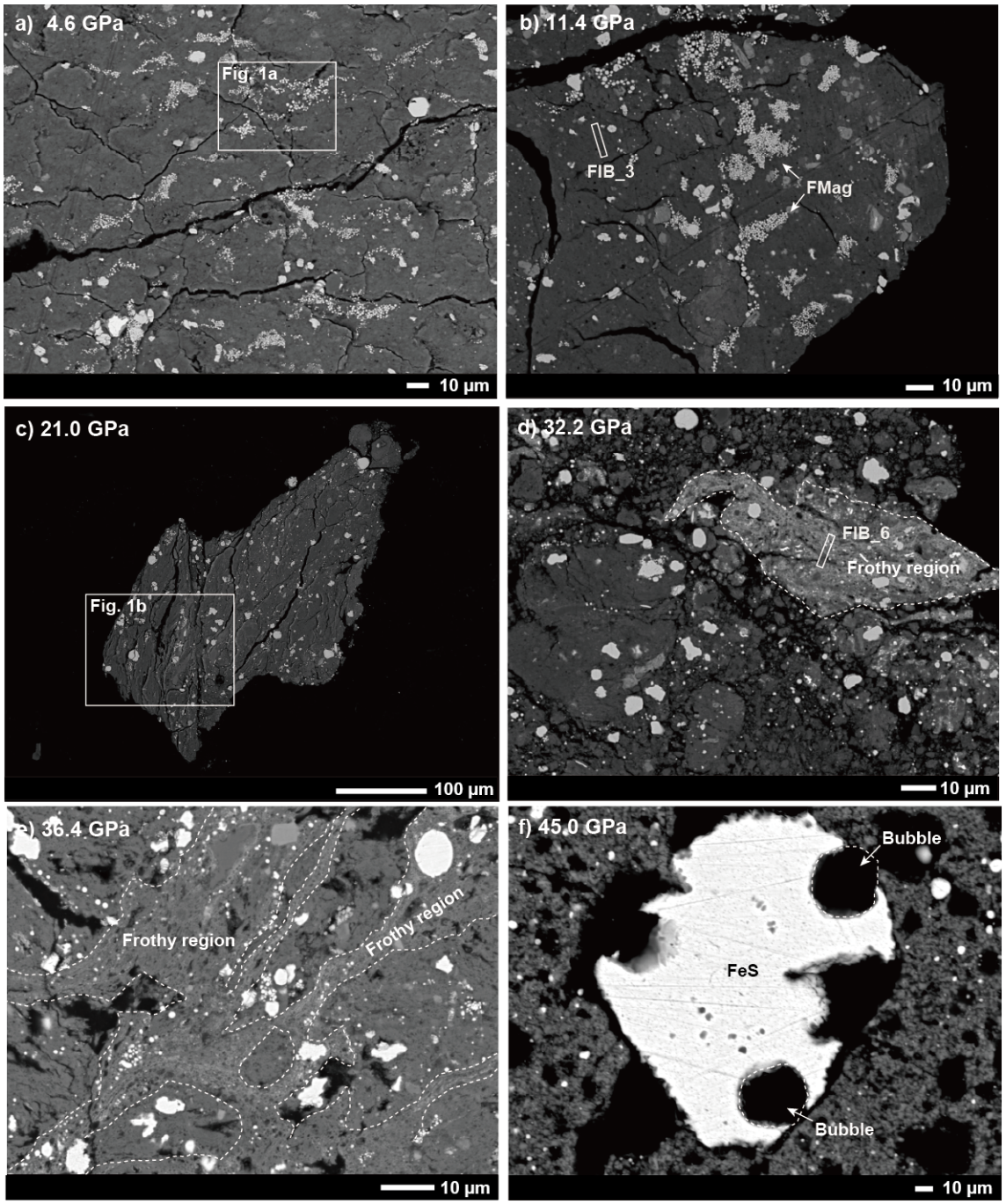

Figure S3. BSE images of Orgueil CI chondrite recovered from shock experiments. a) Magnified image of a white box is shown in Figure 1a. b) Most of FMgs are deformed. c) A magnified image of a white box is shown in Figure 1b. d) A frothy region is observed

in some areas. e) A frothy region occurs as a veinlet in the sample. f) FeS grains have a bubble. The FIB-excavated TEM foil is indicated by a numbered white box. FeS: iron-sulfide, FMg: framboidal magnetite cluster.

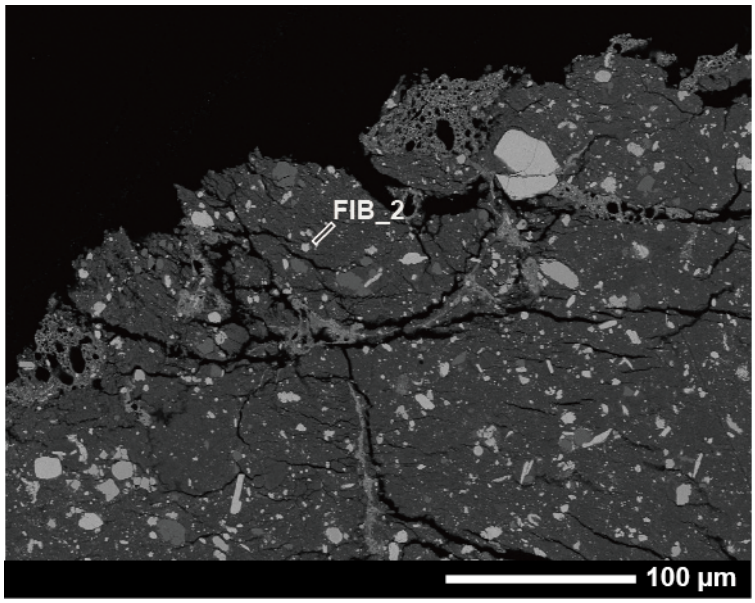

Figure S4. BSE images showing Y 980115 CY chondrite recovered from shock experiments of 22.3 GPa. The FIB-excavated TEM foil is indicated by a numbered white box.

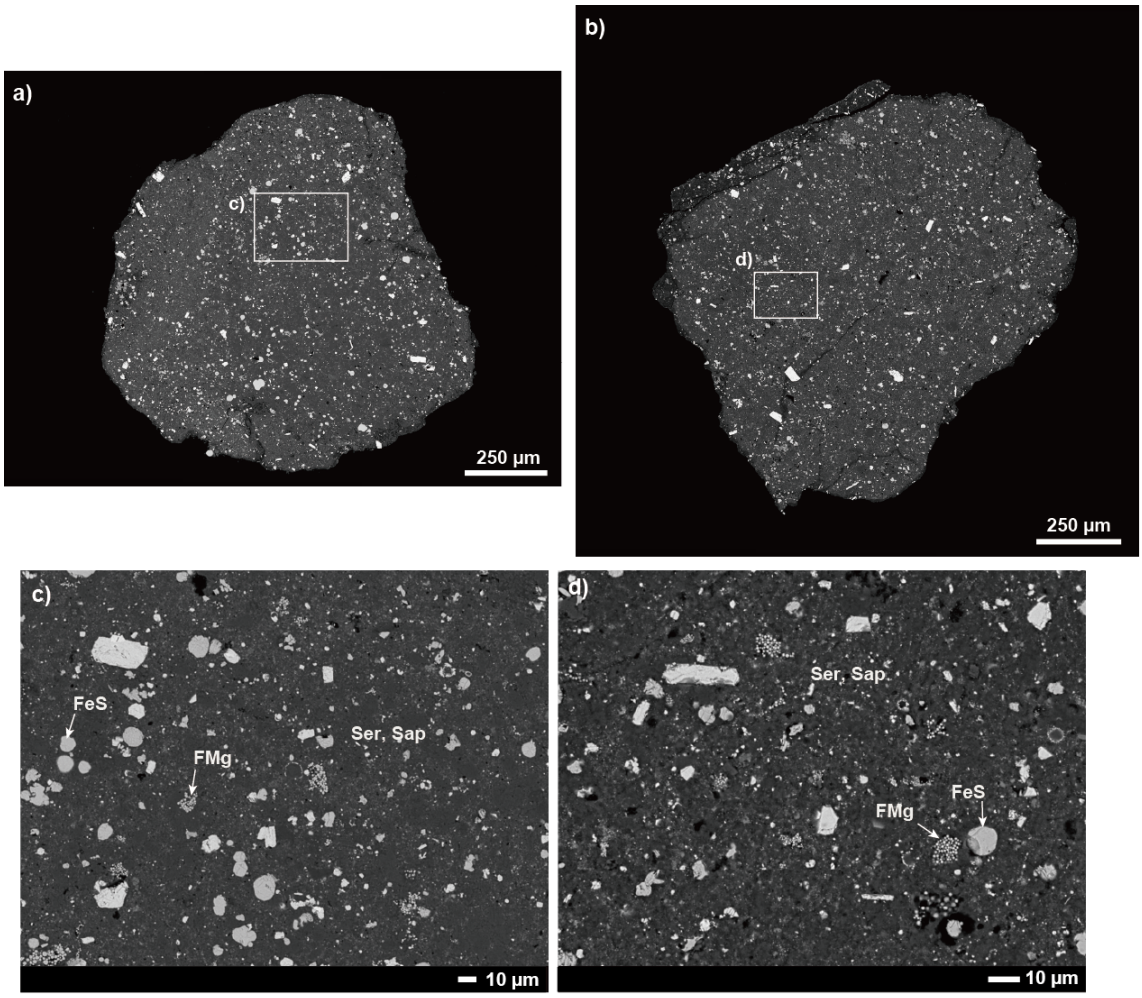

Figure S5. BSE images of a) A0304 and b) C0230 Ryugu grains. c) and d) A magnified image of a white box in a) and b). Sap: saponite, Ser: serpentine, FMg: framboidal magnetite cluster, FeS: iron-sulfide.

Table S1. Crack density and melt area ratio in samples.

Sample name	Shock pressure (GPa)	Crack density (mm^{-2})	Measurement area (mm^2)	Melt area ratio	Measurement area (mm^2)
Orgueil CI	0.0	515	1.232	0.00	1.232
	4.6	910	0.178	0.00	5.325
	11.4	770	1.287	0.00	6.118
	21.0	1609	0.225	0.00	0.340
	32.2	3429	0.338	0.16	1.524
	36.4	942	0.208	0.54	0.220
	40.5	1247	0.085	0.60	0.095
	45.0	-	-	0.79	0.028
Y 980115 CY	0.0	70	143.105	0.00	143.105
	10.7	1037	0.574		
	22.3	1234	0.445	0.14	1.257
	32.5	4495	0.204	0.47	0.239
Ryugu					
A 0304	-	185	0.926	0.00	0.926
C 0055	-	697	0.610	0.00	0.610
C 0230	-	285	1.157	0.00	1.157

-: not determined.